Systematic study of fusion barrier characteristics within the relativistic mean-field formalism

Shilpa Rana,[1,*] M. Bhuyan,[2,†] and Raj Kumar[1,‡]

[1]*School of Physics and Materials Science, Thapar Institute of Engineering and Technology, Patiala 147004, India*

[2]*Department of Physics, Faculty of Science, University of Malaya, Kuala Lumpur 50603, Malaysia*

(Received 19 October 2021; revised 14 March 2022; accepted 9 May 2022; published 25 May 2022)

Background: Heavy-ion fusion reactions play a crucial role in various aspects of nuclear physics and astrophysics. The nuclear interaction potential and hence the fusion barrier formed between the interacting nuclei are the keys to understanding the complex fusion process dynamics. Thus, a theoretical investigation of fusion barrier characteristics which includes the relativistic effects is of paramount significance.

Purpose: This work intends to explore the fusion barrier characteristics of different target-projectile combinations within the relativistic mean-field (RMF) formalism. The M3Y nucleon-nucleon (NN) potential is compared with the relativistic R3Y and density-dependent R3Y (DDR3Y) NN potentials within the double folding approach. A systematic study is carried out to study the effect of different RMF density distributions and effective NN interactions on the fusion and/or capture cross section of 24 target-projectile combinations leading to heavy and superheavy nuclei (SHN).

Methods: The density distributions of interacting nuclei and the microscopic R3Y NN interaction are obtained from the RMF formalism for nonlinear NL1, NL3, and TM1 parameter sets and the relativistic Hartree-Bogoliubov (RHB) approach for the DDME2 parameter set. The medium-independent relativistic R3Y, the density-dependent DDR3Y, and widely adopted M3Y NN potentials are used to obtain the nuclear interaction potential within the double folding approach. The densities for the projectiles and targets are obtained from the relativistic mean-field approaches. The fusion and/or capture cross section for the different reaction systems is calculated using the well-known ℓ-summed Wong model.

Results: The barrier height and position of 24 heavy-ion reaction systems are obtained for different nuclear density distributions and effective NN interaction potentials. We have considered the lighter mass projectile and heavier mass target combinations for synthesizing exotic drip-line nuclei, including the superheavy nuclei (SHN). These reactions include the even-even ^{48}Ca + ^{154}Sm, ^{48}Ca + ^{238}U, ^{48}Ca + ^{248}Cm, and ^{26}Mg + ^{248}Cm; even-odd ^{46}K + ^{181}Ta; odd-odd ^{31}Al + ^{197}Au and ^{39}K + ^{181}Ta; and also 17 other systems for the synthesis of SHN $Z = 120$. The comparison of fusion and/or capture cross section obtained from the ℓ-summed Wong model is made with the available experimental data.

Conclusions: The phenomenological M3Y NN potential is observed to give higher barrier heights than the relativistic R3Y NN potential for all the reaction systems. The comparison of results obtained from different relativistic parameter sets shows that the densities from NL1 and TM1 parameter sets give the lowest and highest barrier heights for all the systems under study. The density dependent DDR3Y NN potential is obtained within the relativistic Hartree-Bogoliubov approach for the DDME2 parameter set. We observed higher barrier heights and lower cross sections for the DDR3Y NN potential as compared to density-independent R3Y NN potentials obtained for considered nonlinear NL1, NL3, and TM1 parameter sets. According to the present analysis, it is concluded that the NL1 and NL3 parameter sets provide comparatively better overlap with the experimental fusion and/or capture cross section than the TM1 and DDME2 parameter sets.

DOI: 10.1103/PhysRevC.105.054613

I. INTRODUCTION

The study of underlying physics involved in low energy heavy-ion fusion reactions is essential for a better understanding of the characteristics of nuclear forces, nuclear structure, superheavy nuclei (SHN), magic shell closure, drip lines, and other related phenomena [1–10]. The interaction potential and consequently the fusion barrier formed between the projectile and target nuclei provide the basis to understand the dynamics involved in these fusion reactions. The characteristics of the fusion barrier such as the barrier height, position, oscillator frequency, etc. are used further to calculate one or more related physical quantities such as the fusion probability and cross section [11–13]. Since the fusion barrier is not a directly measurable quantity in the experiments, theoretical modeling is required to extract its characteristics [14]. The origin of the fusion barrier is the interplay between the attractive

*srana60_phd19@thapar.edu

†bunuphy@um.edu.my

‡rajkumar@thapar.edu

short-range nuclear potential and the repulsive long-range Coulomb potential. The Coulomb potential is a known quantity and has a well-established formula. For the calculation of nuclear potential, we have different theoretical approaches available in the literature [2,15–26]. These theoretical models differ from each other in their basic assumptions and the parameters used. As a consequence, the fusion barrier characteristics calculated also vary and greatly depend upon the adjustments of parameters used in a theoretical formalism [2,15–26].

The phenomenological proximity potentials based on the proximity theorem [16,17] are widely used to estimate the nuclear interaction potential in terms of the mean curvature of the interacting surfaces and a universal function of separation distance [2,16–19]. The Bass potential based upon the liquid drop model also provides a simple exponential form for the nuclear interaction potential [2,20–22]. Moreover, the semimicroscopic approaches describe the nuclear interaction potential as the difference in the energies of interacting nuclei at an infinite separation and a distance when overlapping. Examples include the asymmetric two-center shell model and models based on the energy density formalism (EDF) [23–25,27–31]. Furthermore, the phenomenological double folding approach also has successful applications to deduce the interaction potential between the two colliding heavy ions [32–35]. In this approach, the nuclear optical potential is obtained using nuclear density distributions and effective nucleon-nucleon interaction. The model has been widely adopted to provide real and imaginary parts of the optical potentials between the colliding ions in elastic and inelastic scattering as well as in the study of nuclear fusion characteristics; see Refs. [32–37] and references therein.

Nuclear fusion is considered to be a complex phenomenon since a large number of nucleons are involved. A complete description of the nucleon-nucleon (NN) interaction potential is a prerequisite to understand these nucleon's interactions. One of the well-known approaches to handle the nuclear many-body problem is the self-consistent relativistic mean-field model. Recently, the microscopic R3Y NN interaction potential was also derived from the relativistic mean-field formalism [38–40]. In relativistic mean-field (RMF) models, the pointlike Dirac nucleons interact through the exchange of mesons and photons [36,37,41–47]. The mass of the σ meson and the coupling constants of the interacting mesons are fine tuned to the ground state bulk properties of finite nuclei. A number of these parameter sets are available, with linear and/or nonlinear meson couplings (e.g., HS, models with names starting with L and NL, TM1, FSUGold, IOPB-I, G2, G3, etc.), density-dependent meson-exchange couplings (DDME1, DDME2, DDMEδ, etc.), and zero-range point-couplings (DD-PC1, PC-PK1, etc.); see Refs. [37,38,42–55] and references therein. All these defined parameter sets provide overall satisfactory results for the nuclear bulk properties and also explain the nuclear matter observables [41–44,51–64]. With frequent measurements of various bulk properties from experiments and constraints on nuclear matter observables including highly dense and isospin asymmetric systems, all these relativistic parameters are being developed. Each parametrization in the relativistic mean-field model has its own identities and certain limitations; for more details see Ref. [65]. In the present study, we have considered two different kinds of parametrizations, i.e., nonlinear NL1, NL3, and TM1 parameter sets within the relativistic mean-field model, and the density-dependent DDME2 parameter set within the relativistic Hartree-Bogoliubov (RHB) approach, to study the characteristics of nuclear fusion in terms of the nuclear density distributions and NN potential. The medium-dependent R3Y (named DDR3Y) NN potential given in terms of density-dependent nucleon-meson couplings was recently introduced in a fusion study, and can be found in Ref. [66]. Along with the relativistic R3Y and DDR3Y potentials, we have also employed the widely adopted M3Y potential to estimate the nucleon-nucleon interaction potential [32,33] for comparison.

A systematic analysis will be carried out in three steps to study the effect of nucleon-nucleon interaction potential and the density distributions of the fusing nuclei on the fusion barrier characteristics and consequently on the fusion and/or capture cross section. In the first step, a comparison will be made for the widely used M3Y and recently developed relativistic R3Y effective nucleon-nucleon (NN) potential in terms of nuclear potential within the double folding approach. Moreover, the density-dependent R3Y (DDR3Y) NN interaction potential obtained for the DDME2 parameter set within the RHB approach is also taken into account in this analysis. In the second step, the effect of RMF nuclear density distributions obtained for nonlinear NL1, NL3, TM1 and density-dependent DDME2 parameter sets will be analyzed on the fusion characteristics. Finally, in the third step, we will study the effect of the R3Y NN potential obtained for nonlinear NL1, NL3, and TM1 parameter sets within the RMF model as well as the DDR3Y NN potential obtained for the density-dependent DDME2 parameter set within the RHB approach on the fusion barrier characteristics and consequently on the fusion and/or capture cross section. We have chosen 24 different light mass projectile and heavy mass target combinations from the various exotic regions of the nuclear chart in the present analysis. The even-even ^{48}Ca + ^{154}Sm, ^{48}Ca + ^{238}U, ^{48}Ca + ^{248}Cm, ^{26}Mg + ^{248}Cm; even-odd ^{46}K + ^{181}Ta; and odd-odd ^{31}Al + ^{197}Au and ^{39}K + ^{181}Ta systems of lighter mass projectile and heavier mass target nuclei. These reaction systems involve neutron-rich projectiles and are pertinent for the synthesis of neutron-rich heavy and superheavy nuclei [5,67–71]. Seventeen different possible systems, namely, ^{40}Ca + ^{257}Fm, ^{48}Ca + ^{254}Fm, ^{46}Ti + ^{248}Cf, ^{46}Ti + ^{249}Cf, ^{50}Ti + ^{249}Cf, ^{50}Ti + ^{252}Cf, ^{50}Cr + ^{242}Cm, ^{54}Cr + ^{248}Cm, ^{58}Fe + ^{244}Pu, ^{64}Ni + ^{238}U, ^{64}Ni + ^{235}U, ^{66}Ni + ^{236}U, ^{50}Ti + ^{254}Cf, ^{54}Cr + ^{250}Cm, ^{60}Fe + ^{244}Pu, ^{72}Zn + ^{232}Th, and ^{76}Ge + ^{228}Ra are chosen, leading to the synthesis of different isotopes of highly discussed superheavy $Z = 120$ [41,72,73]. It is worth mentioning that all these isotopes are neutron rich and also ^{304}120 is predicted to be a doubly magic shell nuclei within various theoretical models [41,57,72,74–78]. Hence, it would be of interest to study the effect of different nuclear density distributions and nucleon-nucleon interaction potentials on the fusion and/or capture cross section for these systems. The ℓ-summed Wong model [79] is employed to deduce the fusion and/or capture cross section,

and comparison with the experimental cross section is also made wherever available.

The paper is organized as follows: the theoretical formalism for the nuclear potential using the relativistic mean-field approach and the double folding procedure is explained in Sec. II along with a brief description of the ℓ-summed Wong model to estimate the fusion and/or capture cross section. The results obtained from the calculations are discussed in Sec. III. In Sec. IV the summary and conclusions of the present work are given.

II. NUCLEAR INTERACTION POTENTIAL FROM THE RELATIVISTIC MEAN-FIELD FORMALISM

A complete description of the total interaction potential is crucial to estimate the fusion probability of two colliding nuclei. This interaction potential comprises three parts: the nuclear interaction potential, the Coulomb potential, and the centrifugal potential. The total interaction potential $[V_T^\ell(R)]$ between the projectile and target nuclei can be written as

$$V_T^\ell(R) = V_n(R) + V_C(R) + V_\ell(R). \tag{1}$$

Here, $V_C(R) = Z_p Z_t e^2/R$ and $V_\ell(R) = \frac{\hbar^2 \ell(\ell+1)}{2\mu R^2}$ are the Coulomb and centrifugal potentials, respectively. μ is the reduced mass and R is the separation distance. The nuclear potential $V_n(R)$ is calculated here within the double folding approach [32],

$$V_n(\vec{R}) = \int \rho_p(\vec{r}_p)\rho_t(\vec{r}_t)V_{\text{eff}}(|\vec{r}_p - \vec{r}_t + \vec{R}| \equiv r)d^3r_p d^3r_t. \tag{2}$$

Here, ρ_p and ρ_t are the total density (sum of proton and neutron densities) distributions of projectile and target nuclei, respectively. V_{eff} is the effective nucleon-nucleon (NN) interaction. There are several expressions for the effective NN interaction potential available in the literature. One of the well-known expressions is known as the M3Y (Michigan 3 Yukawa) potential [33]. As the name suggests, it consists of three Yukawa terms [32,33,36,40] and is given by

$$V_{\text{eff}}^{M3Y}(r) = 7999\frac{e^{-4r}}{4r} - 2140\frac{e^{-2.5r}}{2.5r} + J_{00}(E)\delta(r). \tag{3}$$

Here, $J_{00}(E)\delta(r)$ is long-range one-pion exchange potential because there can be the possibility of nucleon exchange between the projectile and target nuclei.

As mentioned before, the characteristics of the total interaction potential play a crucial role in determining the fusion properties. The barrier characteristics such as the barrier height (V_B^ℓ) and barrier position (R_B^ℓ) can be determined from Eq. (1) using following conditions:

$$\left.\frac{dV_T^\ell}{dR}\right|_{R=R_B^\ell} = 0. \tag{4}$$

$$\left.\frac{d^2V_T^\ell}{dR^2}\right|_{R=R_B^\ell} \leqslant 0. \tag{5}$$

Moreover, the barrier curvature $(\hbar\omega_\ell)$ is evaluated at $R = R_B^\ell$ corresponding to the barrier height V_B^ℓ, and is given as

$$\hbar\omega_\ell = \hbar\left[\left|d^2V_T^\ell(R)/dR^2\right|_{R=R_B^\ell}/\mu\right]^{\frac{1}{2}}. \tag{6}$$

To determine these quantities, we need a complete description of nuclear interaction potential, which is calculated here using the double folding integral given by Eq. (2). The main requirements to solve the double folding integral are the nuclear density distributions and effective nucleon-nucleon interaction potential. The well-known relativistic mean-field (RMF) formalism and relativistic-Hartree-Bogoliubov (RHB) have been employed to determine these density distributions and the NN interaction potential. The RMF formalism has its successful applications in describing the properties of nuclear matter as well finite nuclei [36,37,41–45,47–49,56]. A phenomenological description of nucleon interaction through the exchange of mesons and photons is given by the RMF Lagrangian density [36,37,41–45,47–49,56], which can be written as

$$\begin{aligned}\mathcal{L} = {} & \overline{\psi}\{i\gamma^\mu\partial_\mu - M\}\psi + \frac{1}{2}\partial^\mu\sigma\partial_\mu\sigma - \frac{1}{2}m_\sigma^2\sigma^2 \\ & - \frac{1}{3}g_2\sigma^3 - \frac{1}{4}g_3\sigma^4 - g_\sigma\overline{\psi}\psi\sigma - \frac{1}{4}\Omega^{\mu\nu}\Omega_{\mu\nu} \\ & + \frac{1}{2}m_w^2\omega^\mu\omega_\mu + \frac{1}{4}\xi_3(\omega^\mu\omega_\mu)^2 - g_w\overline{\psi}\gamma^\mu\psi\omega_\mu \\ & - \frac{1}{4}\vec{B}^{\mu\nu}.\vec{B}_{\mu\nu} + \frac{1}{2}m_\rho^2\vec{\rho}^\mu.\vec{\rho}_\mu - g_\rho\overline{\psi}\gamma^\mu\vec{\tau}\psi\cdot\vec{\rho}^\mu \\ & - \frac{1}{4}F^{\mu\nu}F_{\mu\nu} - e\overline{\psi}\gamma^\mu\frac{(1-\tau_3)}{2}\psi A_\mu.\end{aligned} \tag{7}$$

Here ψ denotes the Dirac spinor for the nucleons, i.e., proton and neutron. m_σ, m_ω, and m_ρ signify the masses of isoscalar scalar σ, isoscalar vector ω, and isovector vector ρ mesons, respectively which intermediate the interaction between the nucleons having mass M. g_σ, g_ω, and g_ρ are the linear coupling constants of the respective mesons whereas g_2, g_3, and ξ_3 are the nonlinear self-interaction constants for scalar σ and vector ω mesons, respectively. These mass of the σ meson and the coupling constants of mesons are fitted to match the infinite nuclear matter's saturation properties and the bulk properties of magic shell nuclei. For the present study, we have considered three parameter sets, namely NL1 [42], NL3 [43], and TM1 [44]. In NL1 and NL3 parameters, only the σ-meson self-coupling nonlinear terms (i.e, the associated coupling constants, g_2 and g_3) are taken into account. In the case of the TM1 parameter set, the self-coupling term of the vector ω meson (ξ_3) is considered. The terms τ and τ_3 in Eq. (7) symbolize the isospin and and its third component, respectively. $\Omega^{\mu\nu}$, $\vec{B}^{\mu\nu}$, and $F^{\mu\nu}$ are the field tensors for ω, ρ, and photons, respectively and are given as

$$\Omega_{\mu\nu} = \partial_\mu\omega_\nu - \partial_\nu\omega_\mu, \tag{8}$$

$$\vec{B}^{\mu\nu} = \partial_\mu\vec{\rho}_\nu - \partial_\nu\vec{\rho}_\mu, \tag{9}$$

$$F^{\mu\nu} = \partial_\mu A_\nu - \partial_\nu A_\mu. \tag{10}$$

The quantity A_μ here denotes the electromagnetic field, and the arrows symbolize the vectors in the isospin space. The equations of motion for the Dirac nucleon and the mesons are obtained from the Lagrangian density given in Eq. (7) using the Euler-Lagrange equations under mean-field approximation. The field equations for nucleons and mesons (σ, ω, ρ) are given as

$$\begin{aligned}
&(-i\alpha.\nabla + \beta(M + g_\sigma\sigma) + g_\omega\omega + g_\rho\tau_3\rho_3)\psi = \epsilon\psi,\\
&\left(-\nabla^2 + m_\sigma^2\right)\sigma(r) = -g_\sigma\rho_s(r) - g_2\sigma^2(r) - g_3\sigma^3(r),\\
&\left(-\nabla^2 + m_\omega^2\right)\omega(r) = g_\omega\rho(r) - \xi_3\omega^3(r),\\
&\left(-\nabla^2 + m_\rho^2\right)\rho(r) = g_\rho\rho_3(r).
\end{aligned} \tag{11}$$

Note that the terms with σ^3 and σ^4 account for the self-coupling among the scalar σ mesons. Similarly, the term with ω^4 takes care of self-coupling among the vector mesons. These nonlinear self-coupling terms take care of saturation properties and also soften the equation of state of the nuclear matter [39,42–44]. The properties of finite nuclei such as the binding energy and charge radius (r_{ch}) estimated from the Lagrangian density containing the nonlinear σ-ω terms also give a satisfactory match with the experimental values [42–45,47,49,56]. The alternative approach to introduce the density-dependent nucleon-meson couplings within a relativistic mean field is the relativistic-Hartree-Bogoliubov (RHB) approach [53–55,60,61]. In this framework, the couplings of σ, ω, and ρ mesons to the nucleon fields (i.e., g_σ, g_ω and g_ρ) are defined as [53–55,60,61]

$$g_i(\rho) = g_i(\rho_{\rm sat})f_i(x)|_{i=\sigma,\omega}, \tag{12}$$

where

$$f_i(x) = a_i\frac{1 + b_i(x + d_i)^2}{1 + c_i(x + d_i)^2} \tag{13}$$

and

$$g_\rho(\rho) = g_\rho(\rho_{\rm sat})\exp[-a_\rho(x - 1)]. \tag{14}$$

Here, $x = \rho/\rho_{\rm sat}$, with $\rho_{\rm sat}$ being the baryon density of symmetric nuclear matter at saturation. The five constraints- $f_i(1) = 1$, $f_i''(0) = 0$, and $f_\sigma''(1) = f_\omega''(1)$ reduce the number of independent parameters in Eq. (13) from 8 to 3. All the independent parameters (the mass of σ meson and coupling parameters) are obtained to fit the ground state properties of finite nuclei as well as the properties of symmetric and asymmetric nuclear matter. In the present analysis we have adopted the well-known DDME2 parameter set [61] to study the fusion barrier characteristics, and we also compared the results with the ones obtained using nonlinear NL1 [42], NL3 [43], and TM1 [44] parameter sets.

A. Medium-dependent relativistic R3Y potential

The nucleon-nucleon interaction potential analogous to the M3Y potential [see Eq. (3)] has also been derived by solving the mean-field equations in Eq. (11) within the limit of one-meson exchange [37–40]. The relativistic NN potential called the R3Y potential [37–40] can be written as

$$\begin{aligned}
V_{\rm eff}^{R3Y}(r,\rho) = &\frac{[g_\omega(\rho)]^2}{4\pi}\frac{e^{-m_\omega r}}{r} + \frac{[g_\rho(\rho)]^2}{4\pi}\frac{e^{-m_\rho r}}{r}\\
&- \frac{[g_\sigma(\rho)]^2}{4\pi}\frac{e^{-m_\sigma r}}{r} + \frac{g_2^2}{4\pi}re^{-2m_\sigma r}\\
&+ \frac{g_3^2}{4\pi}\frac{e^{-3m_\sigma r}}{r} - \frac{\xi_3^2}{4\pi}\frac{e^{-3m_\omega r}}{r} + J_{00}(E)\delta(r).
\end{aligned} \tag{15}$$

It is worth mentioning here that for the case of the medium-independent R3Y NN potential obtained for NL1, NL3, and TM1 parameter sets, the nucleon-meson couplings (g_σ, g_ω, and g_ρ) appearing in Eq. (15), are independent of the density. However, in the case of the medium-dependent DDR3Y NN potential for the DDME2 parameter set, the g_σ, g_ω, and g_ρ are density dependent [given in Eqs. (12)–(14)] and also the non-linear self-interaction constants (g_2, g_3, ξ_3) are zero for DDR3Y. The density (ρ) entering in Eqs. (12)–(15) is obtained within the relaxed density approximation (RDA) [80,81] at the midpoint of the internucleon separation distance and can be written as

$$\begin{aligned}
\rho\left(\frac{\vec r}{2}\right) = &\rho_p\left(\vec r_p + \frac{\vec r}{2}\right) - \frac{2\rho_{N_p}(\vec r_p + \frac{\vec r}{2})\rho_{N_t}(\vec r_t - \frac{\vec r}{2})}{\rho_{1_N} + \rho_{2_N}}\\
&+ \rho_t\left(\vec r_t - \frac{\vec r}{2}\right) - \frac{2\rho_{P_p}(\vec r_p + \frac{\vec r}{2})\rho_{P_t}(\vec r_t - \frac{\vec r}{2})}{\rho_{1_P} + \rho_{2_P}}.
\end{aligned} \tag{16}$$

Here, ρ_{N_p} (ρ_{P_p}) and ρ_{N_t} (ρ_{P_t}) are the neutron (proton) densities of projectile and target nuclei, respectively. Also, $\rho_{1(2)_N} = \frac{N_{p(t)}}{A_{p(t)}}\rho_{\rm sat}$ and $\rho_{1(2)_P} = \frac{Z_{p(t)}}{A_{p(t)}}\rho_{\rm sat}$, with $N_{p(t)}$ and $A_{p(t)}$ being the neutron and mass numbers of projectile (target) nuclei, respectively. More details about the validity of this RDA in obtaining the DDR3Y NN potential can be found in one of our recent works [66], where a comprehensive analysis of the fusion cross section obtained using density-dependent M3Y [32,82,83] and R3Y NN potentials is accomplished. In the present analysis, a systematic study of fusion barrier characteristics obtained using different RMF density distributions, relativistic R3Y, DDR3Y, and nonrelativistic M3Y NN potentials is done for 24 isospin asymmetric reaction systems forming heavy and superheavy nuclei. In open-shell nuclei, the pairing plays a significant role in describing their structure properties, including the density distributions. In the present study, we have considered the nuclei near the β-stable region of the nuclear chart, so we have considered simple BCS pairing to take care of the pairing correlations [36,37,84,85]. Also, a blocking procedure is used to treat the odd-mass-number nuclei [36,37,86,87].

The relativistic R3Y NN potential for different parameter sets and the analogous M3Y potential are shown in Fig. 1. The R3Y NN potential for DDME2 is plotted here for the coupling constants in Eq. (15) at the saturation density, $\rho_{\rm sat} = 0.152$ fm^{-3} [61]. It can be observed from Fig. 1 that the curves for

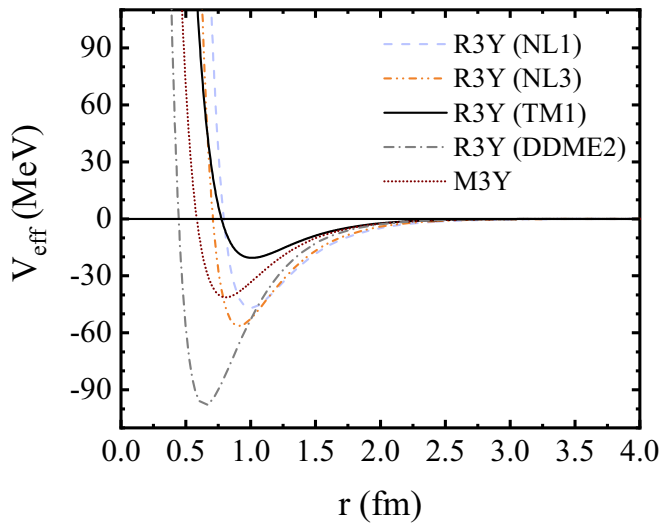

FIG. 1. The relativistic R3Y NN potential for NL1 (dashed light blue line), NL3 (dash–double-dotted orange line), TM1 (solid black line), and DDME2 (dash-dotted grey line) parameter sets are compared with the phenomenological M3Y NN-interaction potential (dotted dark red line). The R3Y NN potential for DDME2 is plotted at saturation density ($\rho_{sat} = 0.152$ fm^{-3} for DDME2 [61]).

the R3Y NN-interaction potential for NL1, NL3, TM1, and DDME2 parameter sets show similar trends as the M3Y NN potential. The R3Y NN potential for the DDME2 parameter set at saturation density is observed to show the deepest pocket. However, the actual DDR3Y NN potential for the DDME2 parameter used to obtain the nuclear potential within the double-folding approach is density dependent and is not exactly similar to one plotted at $\rho_{sat} = 0.152$ fm^{-3} in Fig. 1. A more detailed inspection shows that the R3Y NN potential for NL3 and NL1 parameter sets shows a slightly deep pocket compared to M3Y NN potential. However, the R3Y potential for the TM1 parameter shows a lightly shallow pocket compared to the M3Y potential, which can be connected with the self-coupling nonlinear term (ξ_3) in the ω-field. More details can be found in Refs. [37–40]. The barrier characteristics of total interaction potential given in Eq. (1) are used further to obtain the fusion and/or capture cross section using the ℓ-summed Wong model.

B. ℓ-summed Wong model

The fusion and/or capture cross section for two colliding nuclei is given in terms of the ℓ partial wave by [36,37,79,88]

$$\sigma(E_{c.m.}) = \frac{\pi}{k^2}\sum_{\ell=0}^{\ell_{max}}(2\ell+1)P_\ell(E_{c.m.}). \tag{17}$$

Here, $E_{c.m.}$ is the center-of-mass energy of the target-projectile system and $k = \sqrt{\frac{2\mu E_{c.m.}}{\hbar^2}}$. P_ℓ is called the penetration probability, which describes the transmission through the barrier given in Eq. (1). Using the Hill-Wheeler [89] approximation, P_ℓ can be written in terms of barrier height (V_B^ℓ) and curvature ($\hbar\omega_\ell$) as

$$P_\ell = \left[1 + \exp\left(\frac{2\pi(V_B^\ell - E_{c.m.})}{\hbar\omega_\ell}\right)\right]^{-1}. \tag{18}$$

Equation (17) describes the fusion and/or capture cross section of two interacting nuclei in terms of summation over ℓ partial waves. Wong [88] replaced this summation by integration using the following approximations: (i) $\hbar\omega_\ell \approx \hbar\omega_0$ and (ii) $V_B^\ell \approx V_B^0 + \frac{\hbar^2\ell(\ell+1)}{2\mu R_B^{0\,2}}$, assuming $R_B^\ell \approx R_B^0$. These approximations lead to a simple formula to estimate the fusion and/or capture cross section in terms of barrier characteristics. This simplified Wong formula [88] can be written as

$$\sigma(E_{c.m.}) = \frac{R_B^{0\,2}\hbar\omega_0}{2E_{c.m.}} ln\left[1 + \exp\left(\frac{2\pi}{\hbar\omega_0}(E_{c.m.} - V_B^0)\right)\right]. \tag{19}$$

However, using only the $\ell = 0$ barrier and ignoring the modifications entering due to ℓ dependence of the potential cause the overestimation of fusion and/or capture cross section by the Wong formula at above-barrier energies. Gupta and collaborators gave the solution of this problem [36,37,79] by using the more precise ℓ-summed formula given in Eq. (17).

III. CALCULATIONS AND DISCUSSION

In this section, the fusion and/or capture cross section of heavy-ion reactions is studied within the ℓ-summed Wong model supplemented with the self-consistent relativistic mean-field and relativistic Hartree-Bogoliubov formalism. As we know, the values of nuclear matter observables and the structural properties of finite nuclei obtained from the RMF and RHB formalism depend upon the force parameter set. Parallel to this, the dependence of fusion characteristics upon these RMF parameter sets can be anticipated. In the present analysis, we systematically study the nuclear density distributions and the effective nucleon-nucleon interaction potential dependence on the different parameter sets and, consequently, on the fusion barrier characteristics. The nuclear density distributions for all the interacting nuclei (targets and projectiles) are obtained within the relativistic mean-field formalism for three force parameter sets NL1, NL3, and TM1, and within the relativistic Hartree-Bogoliubov approach for the DDME2 parameter set. We have considered three types of effective nucleon-nucleon interactions: (i) the widely used nonrelativistic M3Y potential given by Eq. (3); (ii) the density-independent relativistic R3Y NN potential described in terms of masses and coupling constants of the mesons (σ, ω, and ρ mesons). The medium-independent relativistic R3Y potential is obtained for three relativistic parameter sets, i.e., NL1, NL3, and TM1. (iii) The medium dependence of the R3Y NN potential is also taken into account via density-dependent meson-nucleon coupling terms obtained from the DDME2 parameter set.

From Fig. 1, it can be noted that the NN potentials of M3Y and R3Y for NL1, NL3, TM1, and DDME2 sets show a similar trend but with different depths. A systematic study

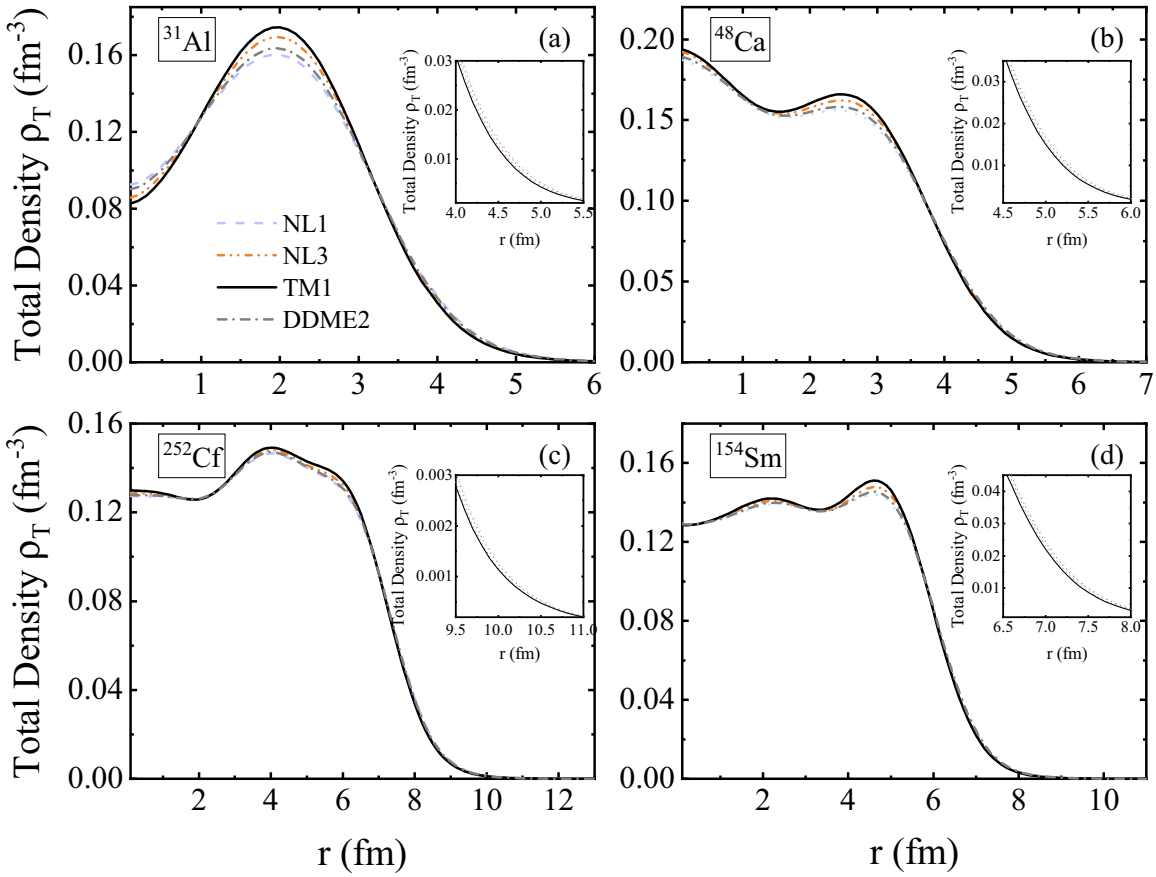

FIG. 2. The variation of total density distributions as a function of nuclear radius r (fm) for (a) ^{31}Al, (b) ^{48}Ca, (c) ^{252}Cf, and (d) ^{154}Sm nuclei calculated using RMF with NL1 (light blue), NL3 (orange), TM1 (black), and DDME2 (grey) parameter sets. Insets shows the magnified view of tail region of the densities. See text for details.

is carried out to study the effect of these NN interactions on the nuclear potential (V_n) calculated within the double folding approach. As mentioned above, the R3Y NN potential for the DDME2 parameter is plotted at saturation density ($\rho_{\rm sat} = 0.152$ fm^{-3}) in Fig. 1 whereas the actual density-dependent R3Y (DDR3Y) obtained within the RHB approach is used for calculating the nuclear potential and the fusion and/or capture cross section. The calculations are done in three steps: (i) The nuclear density distributions are folded with the medium-independent relativistic R3Y potential for three parameters sets NL1, NL3, and TM1 and the DDR3Y NN potential for the DDME2 parameter set to obtain the nuclear potential. The nuclear density distributions are also folded with the phenomenological M3Y potential for the comparison. (ii) In the second step, the R3Y NN potential is fixed for one parameter set and is folded with the density distributions obtained with the considered four parameter sets. (iii) In the last step, the density is fixed for one parameter set and is folded with the R3Y NN potential obtained for NL1, NL3, TM1, and DDME2 parameter sets.

Nuclear density distributions. The RMF formalism successfully describes bulk properties such as the binding energy, quadrupole deformations, nuclear density distributions, etc., throughout the nuclear chart. The total density (sum of the proton and neutron number densities, i.e., $\rho_T = \rho_P + \rho_N$) as a function of nuclear radius (r) is plotted in Fig. 2 for the representative cases of (a) odd-mass ^{31}Al, (b) even-mass light ^{48}Ca, (c) heavy ^{252}Cf, and (d) intermediate ^{154}Sm nuclei. These density distributions are obtained by solving the RMF equations for the NL1 (dashed light blue line), NL3 (dash–double-dotted orange line), and TM1 (solid black line) parameter sets and within the RHB approach for the DDME2 (dash-dotted grey line) parameter set. It can be observed from Fig. 2(a) that the density of the odd-mass light ^{31}Al nucleus shows a peak in the central region whereas the density of the ^{48}Ca nucleus shows a downturn in the central region which is caused by the combined effects of Coulomb repulsion and the nuclear shell structure [90–92]. Moreover, the density distributions of intermediate and heavy mass target nuclei show a comparatively flattened curve in the central region that falls rapidly in the surface region. The figure shows that NL1 and TM1 have respectively, the lowest and highest magnitudes of central density for all the nuclei under study. In the case of the heavy-ion fusion reactions, the density at the tail/surface region only plays the most crucial role in the fusion process [93]. The insets in Fig. 2 show the magnified view of the tail region of the densities. A slight difference is observed among the NL1, NL3, TM1, and DDME2 density distributions at the surface/tail region of all the interacting nuclei. A systematic and quantitative study is carried out in the upcoming

subsections to analyze the effects of this slight difference on the fusion characteristics.

A. Folding RMF densities with R3Y, DDR3Y, and M3Y NN potentials

In the first analysis, a comparison is made between the widely adopted nonrelativistic M3Y, density-independent relativistic R3Y, and density-dependent relativistic R3Y (DDR3Y) NN potentials within the double folding approach. The RMF nuclear density distributions obtained for nonlinear NL1, NL3, TM1, and density-dependent DDME2 parameter sets (see Fig. 2) are folded with the M3Y, R3Y, and DDR3Y NN potentials to obtain the nuclear optical potential. In our earlier work, the density-independent M3Y and R3Y nucleon-nucleon potentials were used to study the fusion hindrance phenomenon in a few Ni-based reactions [36] and to study the cross section for the synthesis of heavy and superheavy nuclei [37,94]. In [36,37], the fusion and/or capture cross section obtained using the nonrelativistic M3Y NN potential is compared with the relativistic R3Y NN potential for the NL3* parameter set only. A more systematic study with the inclusion of different nonlinear RMF parameter sets as well as the explicit medium dependence of the R3Y NN potential is carried out in the present analysis to investigate the effect of different nucleon-nucleon potentials and the nuclear density distributions on the fusion and/or capture cross section of 24 different exotic reaction systems. The reaction system involves the projectile with a higher N/Z ratio synthesizing neutron-rich heavy and superheavy nuclei. We have considered 17 target-projectile combinations for the synthesis of different isotopes of SHN with $Z = 120$. The fusion barrier characteristics (barrier height, barrier position, frequency, etc.) are obtained within the double folding approach for both M3Y and R3Y NN potentials. Then the fusion and/or capture cross section is calculated from the well-known ℓ-summed Wong model.

1. Total interaction potential

As discussed above, the interaction potential at $\ell = 0\hbar$ (sum of nuclear and Coulomb potentials) formed between the target and projectile nuclei plays the most crucial role in determining the fusion characteristics of the system. We have calculated the nuclear interaction potential from nuclear density distributions integrated over M3Y, R3Y, and DDR3Y effective NN interactions. The total interaction potential at $\ell = 0\hbar$ $[V_T(R) = V_n(R) + V_C(R)]$ is obtained for the even-even ^{48}Ca + ^{154}Sm, ^{48}Ca + ^{238}U, ^{48}Ca + ^{248}Cm, ^{26}Mg + ^{248}Cm; even-odd ^{46}K + ^{181}Ta; and odd-odd ^{31}Al + ^{197}Au and ^{39}K + ^{181}Ta systems, and also for 17 systems for the synthesis of SHN $Z = 120$: ^{40}Ca + ^{257}Fm, ^{48}Ca + ^{254}Fm, ^{46}Ti + ^{248}Cf, ^{46}Ti + ^{249}Cf, ^{50}Ti + ^{249}Cf, ^{50}Ti + ^{252}Cf, ^{50}Cr + ^{242}Cm, ^{54}Cr + ^{248}Cm, ^{58}Fe + ^{244}Pu, ^{64}Ni + ^{238}U, ^{64}Ni + ^{235}U, ^{66}Ni + ^{236}U, ^{50}Ti + ^{254}Cf, ^{54}Cr + ^{250}Cm, ^{60}Fe + ^{244}Pu, ^{72}Zn + ^{232}Th, and ^{76}Ge + ^{228}Ra. Figure 3 shows the barrier region of the total interaction potential (MeV) at $\ell = 0\hbar$ as a function of the radial separation R (fm) for all 24 reaction systems. The dashed lines signify the phenomenological M3Y NN potential integrated over the nuclear densities obtained for NL1 (light blue), NL3 (orange), TM1 (black), and DDME2 (grey) parameter sets. However, the solid lines signify the relativistic R3Y and DDR3Y potentials along with the mean-field densities used to obtain the nuclear potential within the double folding approach.

From Fig. 3, one can notice that the M3Y NN potential gives a relatively higher barrier as compared to the relativistic R3Y and DDR3Y NN potentials for all the considered systems. This signifies that the microscopic R3Y effective NN potential given in terms of the meson masses and their coupling constants gives a comparatively more attractive interaction potential than the M3Y NN potential, described as the sum of three Yukawa terms. Comparing the barrier heights for different density distributions (NL1, NL3, TM1, and DDME2) folded with the M3Y potential, it is observed that TM1 and NL1 sets give the highest and lowest barrier heights, respectively. For the case of the M3Y NN potential, the NL3 and TM1 densities are observed to give a higher barrier than the DDME2 parameter set whereas for the case of the R3Y NN potential the DDME2 set gives the highest barrier. This is because the R3Y NN potential for the DDME2 parameter is density dependent. The relaxed density approximation (RDA) is used here to include the density dependence of the microscopic R3Y NN potential in terms of nucleon-meson couplings. Thus, the barrier height is observed to be increased with the inclusion of the in-medium effects of the R3Y NN potential.

The Bass potential [20–22] is a simpler and well-known form of nuclear potential. Here, we have studied the variation in fusion barrier characteristics, i.e., barrier height V_B and position R_B obtained from M3Y, R3Y, and DDR3Y NN potentials with respect to (w.r.t.) those obtained from the Bass potential. Figure 4 shows the percentage change in barrier height (upper panel) and barrier position (lower panel) as a function of charges Z_pZ_t for all 24 systems. Here, Z_p and Z_t are atomic numbers for projectile and target nuclei, respectively. M3Y-NL1, M3Y-NL3, M3Y-TM1, and M3Y-DDME2 signify that the nuclear density distributions obtained for nonlinear NL1, NL3, TM1 and density-dependent DDME2 parameter sets, respectively, along with the M3Y NN potential, are used within the double folding procedure to calculate the nuclear potential. Similarly, NL1-NL1, NL3-NL3, and TM1-TM1 signify that the RMF density distributions and relativistic R3Y NN potential are used within the double folding approach to obtain the nuclear potential. Also, DDME2-DDME2 signifies that the DDR3Y NN potential and density distributions obtained within the RHB approach for the DDME2 parameter set are used to calculate the nuclear potential. The Coulomb potential is added then to this nuclear potential and the barrier characteristics (V_B, R_B) are obtained using Eqs. (4) and (5). It can be noted from Fig. 4 that the nuclear potential calculated for the M3Y NN potential shows $\leqslant$2% change in barrier height and $\leqslant$1% change in barrier position for the considered reactions w.r.t. the Bass potential. However, in the case of the nuclear potential obtained for R3Y and DDR3Y NN potentials, the barrier height decreases by up to $\approx$5% and the barrier position shifts by up to $\approx$8%

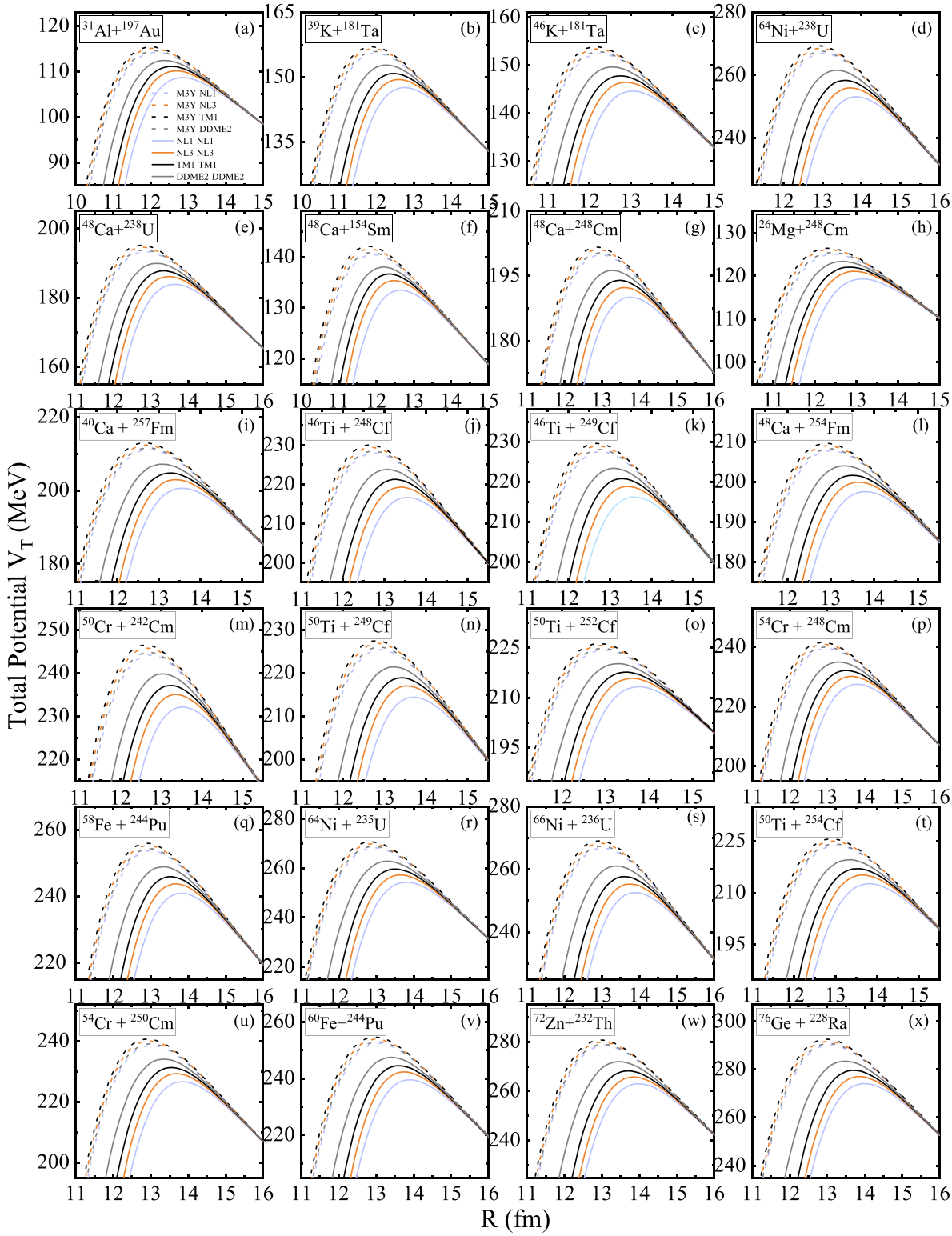

FIG. 3. The total interaction potential V_T (MeV) at $\ell = 0\hbar$ as a function of radial separation R for 24 reaction systems under study calculated using the M3Y (dashed lines), R3Y, and DDR3Y (solid lines) NN potentials. The different colors are for parameter sets as labeled in the figure. See text for details.

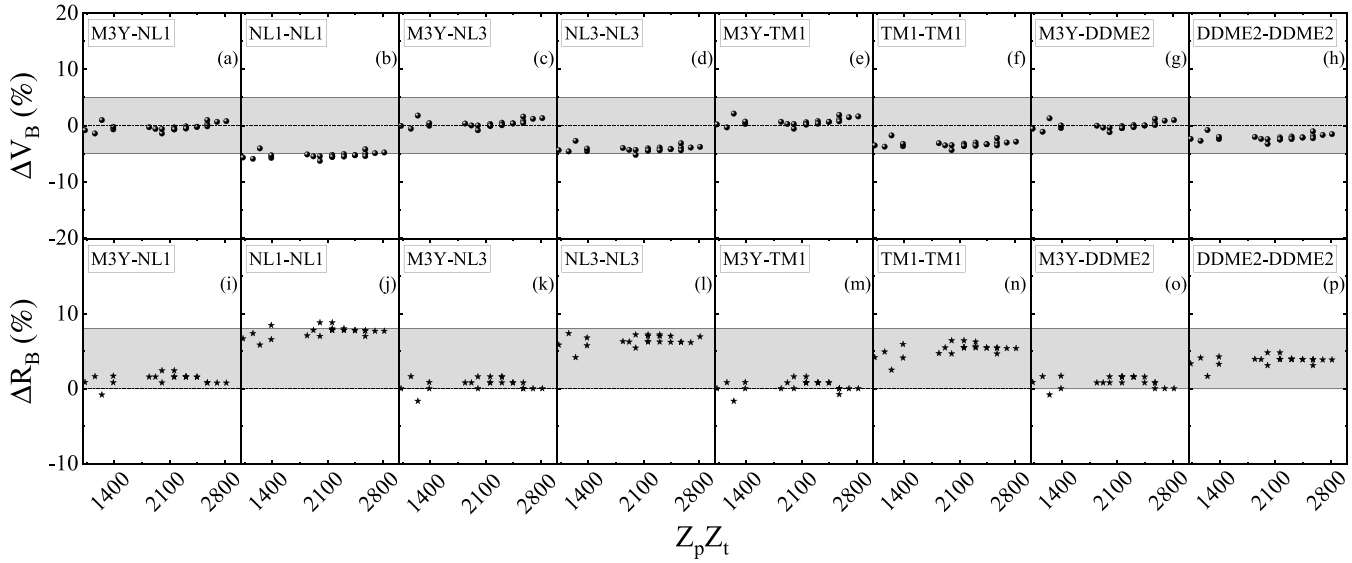

FIG. 4. The percentage (%) change in barrier height (upper panel) and barrier position (lower panel) as a function of charges Z_pZ_t for all the 24 reaction systems under study. See text for details.

towards the higher separation distance w.r.t. the Bass potential. Moreover, this percentage change in barrier characteristics is minimum for the nuclear density distributions obtained for the TM1 parameter set and is maximum for those for the NL1 parameter set. This shows that the inclusion of vector meson self-coupling term ($\propto \omega^4$) in the RMF Lagrangian results in the stronger repulsive core of the NN interaction potential. The characteristics of the fusion barrier have a direct impact on the fusion cross section of the reaction systems. The higher the barrier height value calculated for a system, the lower will be its cross section. The effect of different RMF densities and the NN interaction potential on the fusion and/or capture cross section is studied using the well known ℓ-summed model in the following subsection.

2. *Fusion and/or capture cross section*

The characteristics of the total interaction potential (barrier height, position, and frequency) are further used to estimate the fusion probability and cross section. We have calculated the fusion and/or capture cross section for all 24 reaction systems within the well-known ℓ-summed Wong model described in detail in the previous section. Figure 5 shows the cross section σ (mb) as function of center-of-mass energy $E_{\text{c.m.}}$ (MeV) for all the target-projectile systems including the even-even ^{48}Ca + ^{154}Sm, ^{48}Ca + ^{238}U, ^{48}Ca + ^{248}Cm, ^{64}Ni + ^{238}U, ^{26}Mg + ^{248}Cm; even-odd ^{46}K + ^{181}Ta; and odd-odd ^{31}Al + ^{197}Au and ^{39}K + ^{181}Ta systems. We have also considered here 17 different target-projectile combinations which lead to the synthesis of SHN $Z = 120$: ^{40}Ca + ^{257}Fm, ^{48}Ca + ^{254}Fm, ^{46}Ti + ^{248}Cf, ^{46}Ti + ^{249}Cf, ^{50}Ti + ^{249}Cf, ^{50}Ti + ^{252}Cf, ^{50}Cr + ^{242}Cm, ^{54}Cr + ^{248}Cm, ^{58}Fe + ^{244}Pu, ^{64}Ni + ^{238}U, ^{64}Ni + ^{235}U, ^{66}Ni + ^{236}U, ^{50}Ti + ^{254}Cf, ^{54}Cr + ^{250}Cm, ^{60}Fe + ^{244}Pu, ^{72}Zn + ^{232}Th, and ^{76}Ge + ^{228}Ra. The calculated fusion and/or capture cross section is also compared with the available experimental data [5,67–71]. The $\ell_{\max}$ values are calculated using the sharp cut-off model [95] for the reaction systems with experimental data. Since the experimental fusion and/or capture cross section is not available for all the systems leading to the formation of SHN $Z = 120$ except the ^{64}Ni + ^{238}U reaction [71], the sharp cut-off model is not applicable for them. To extract the $\ell_{\max}$ values for these system we have used the polynomial between $E_{\text{c.m.}}/V_B$ and $\ell_{\max}$ values constructed using ^{64}Ni + ^{238}U data in our earlier work [94]. The dashed lines in Fig. 5 show the cross section estimated by employing the nuclear potential calculated by folding the M3Y NN interaction over the nuclear density distribution obtained for NL1 (light blue), NL3 (orange), TM1 (black), and DDME2 (grey) parameter sets. The solid lines in Fig. 5 signify that the nuclear potential calculated by folding the relativistic R3Y and DDR3Y NN potentials along with the spherical densities obtained for NL1 (light blue), NL3 (orange), TM1 (black), and DDME2 (grey) parameter sets is employed to calculate the cross section.

It can be observed from Fig. 5 that the R3Y and DDR3Y NN interaction potentials give much better overlap with the experimental data as compared to the M3Y NN interaction for all the reaction systems. Comparing the cross sections from different relativistic force parameter sets, we find that the DDME2 parameter set gives the lowest whereas the NL1 set gives the highest cross-section value for a given system. However, this difference is more evident below and around the fusion barrier center-of-mass energies. At above-barrier energies, the cross sections from all the parameter sets almost overlap. The reason for this behavior is that the structure effects get diminished at above-barrier energies, and the angular momentum part of total potential dominates [36]. Comparison of the results for different relativistic parameter sets with the experimental data shows that the NL1 parameter set is superior to the NL3, TM1 and DDME2 parameter sets. Out of NL3, TM1, and DDME2 sets, the parameter set NL3 is observed to fit the experimental data better. This is because the TM1 parameter set, which includes the self-coupling terms of

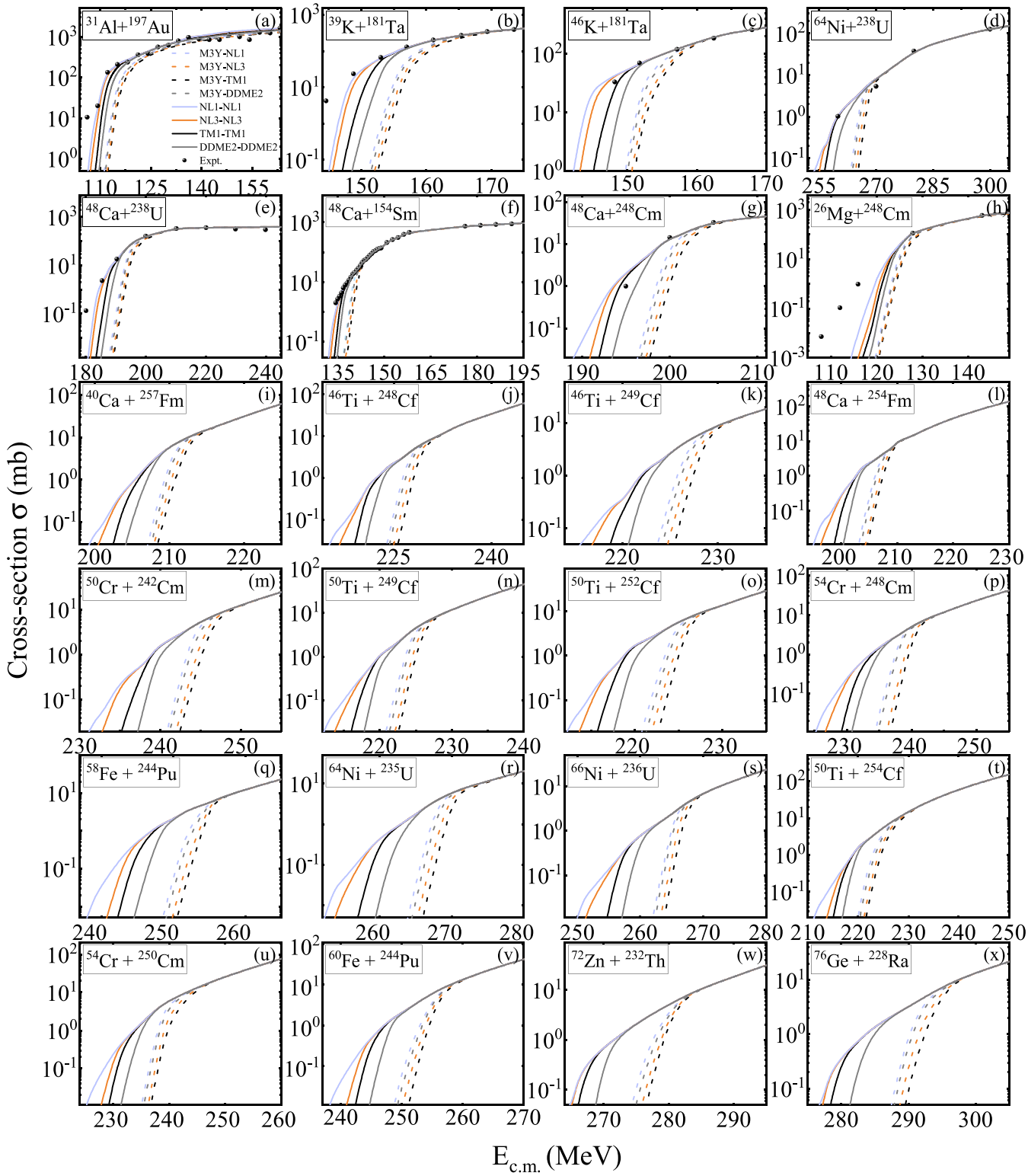

FIG. 5. The cross section σ (mb) for all target projectile combinations considered in the present study by using M3Y (dashed lines) and R3Y (solid lines) interaction using NL1 (light blue), NL3 (orange), TM1 (black), and DDME2 (grey) parameter sets. The solid black circle indicates the experimental data [5,67–71]. See text for details.

the ω mesons, gives a comparatively repulsive NN interaction, underestimating the fusion and/or capture cross section. However, for three reactions, namely ^{46}K + ^{181}Ta [Fig. 5(b)], ^{64}Ni + ^{238}U [Fig. 5(d)], and ^{48}Ca + ^{248}Cm [Fig. 5(g)], TM1 give better overlap than the other parameter sets. Moreover, the DDME2 density folded with M3Y is observed to give a higher cross section than NL3 and TM1 densities. In contrast, the DDME2 density folded with the DDR3Y NN potential

gives a lower cross section than the R3Y NN potential folded with NL1, NL3, and TM1 densities. This indicates that the inclusion of the density dependence of the microscopic R3Y NN potential in terms of the DDME2 parameter set decreases the cross section. In the case of the system ^{26}Mg + ^{248}Cm [Fig. 5(h)], both the M3Y as well as R3Y NN potentials underestimate the experimental cross section at below-barrier energies. This deviation between the experimental and theoretically calculated cross sections is caused by the fusing nuclei's structural deformations, which are not considered in the present study.

In the case of the reaction systems leading to the formation of different isotopes of SHN with $Z = 120$, the experimental data are only available for ^{64}Ni + ^{238}U and, as discussed above, shows a good overlap with the results obtained with the R3Y NN interaction for TM1 parameter sets. Among all the systems for $Z = 120$, the difference between cross sections obtained for NL1, NL3, TM1, and DDME2 parameters sets is comparatively a little more prominent for ^{58}Fe + ^{244}Pu [see Fig. 5(v)] system. In the case of the ^{26}Mg + ^{248}Cm system, the experimental data are available at center-of-mass energies far below its Bass barrier (at 126.833 MeV). For the ^{48}Ca + ^{248}Cm system, the R3Y NN potential for TM1 gives a better fit to the experimental data as compared to other systems. From all these observations, a more systematic investigation of the effects of NN potential and RMF density distributions on the cross section is carried only for these three reaction systems in the upcoming subsections. We have dropped the M3Y NN potential for further investigation of fusion characteristics as it gives comparatively poor overlap with the experimental data. Since the NL1 and NL3 RMF parameter sets give comparatively better results than the TM1 parameter sets, we fix the NN R3Y potential and RMF density distribution for second and third steps for these parameter sets to explore their effects on the fusion characteristics.

B. Fixing the relativistic R3Y NN interaction and varying the density

After comparison of the barrier characteristics and fusion and/or capture cross section obtained from nonrelativistic M3Y and relativistic R3Y and DDR3Y NN interaction potentials, next we investigate the effects of RMF nuclear density distributions obtained from different force parameter sets on fusion characteristics. In Fig. 2, one notices a small difference at the surface region of interacting nuclei among the nuclear densities given by NL1, NL3, TM1, and DDME2 parameter sets. Since nuclear fusion is a surface phenomenon, the tail region of density distributions plays the most crucial role in the fusion cross section [93]. To study the effect of density distributions on the nuclear potential and consequently on the fusion characteristics, we fixed the effective NN interaction in the double folding approach and then changed the densities of the fusing nuclei. First, we fixed the relativistic R3Y NN potential for the NL1 parameter set and folded it with the density distributions obtained for NL1, NL3, TM1, and DDME2 parameter sets to estimate the nuclear potential from Eq. (2). Then the same procedure was repeated for the R3Y NN potential obtained for the NL3 parameter set. The total interaction potential in terms of barrier height and position and the fusion and/or capture cross section were then investigated for different density distributions.

1. Total interaction potential

The total interaction potential is calculated for all the nuclear potentials using the same procedure described in the previous subsection. The barrier region of the total interaction potential as a function of radial separation is represented in Fig. 6 for the systems (a) ^{48}Ca + ^{248}Cm, (b) ^{26}Mg + ^{248}Cm, and (c) ^{58}Fe + ^{244}Pu. The values of V_B and R_B for all 24 reaction systems are given in Table I. Here NL3-TM1 signifies that the R3Y NN interaction potential obtained for the NL3 parameter set is folded with the RMF density distributions obtained for the TM1 parameter set. Similarly, NL1-NL3 signifies that the R3Y NN interaction potential obtained for the NL1 parameter set is folded with the RMF density distributions obtained for the NL3 parameter set. The same notation will be used in all the figures and their discussion from here onwards. The inspection of Fig. 6 and Table I shows that out of eight possible nuclear potentials the ones with TM1-NL3 and NL1-NL1 give the highest and lowest fusion barriers, respectively. Comparing the characteristics of the barrier for NL1-NL1, NL1-NL3, NL1-TM1, and NL1-DDME2 with the same effective NN interaction potential, we find that the densities obtained for NL3, TM1, and DDME2 parameter sets raise the fusion barrier as compared to NL1. The barrier height increases by ≈1 MeV, and the barrier position shifts by ≈0.1 fm towards the lower radial distance as we replace the NL1 densities with those of NL3. Similar behavior is also observed for the nuclear potentials for NL3-NL3, NL3-NL1, NL3-TM1, and NL3-DDME2. In a nutshell, the density distribution obtained for the TM1 parameter set gives the highest fusion barrier, and those for the NL1 parameter sets give the lowest fusion barrier. The density distributions given by NL1 parameter sets were observed to be more extended in the surface region than NL3, TM1, and DDME2 densities. It can be inferred from here that a small increase in the densities of fusing nuclei at the surface region lowers the barrier height by approximately 1 MeV. The suppression of barrier height will enhance the fusion and/or capture cross section around the barrier center-of-mass energies. To study the effect of density distributions more clearly further, we have calculated the fusion and/or capture cross section using all six nuclear potentials given in Fig. 6 and listed in Table I.

2. Fusion and/or capture cross section

To investigate the effects of RMF nuclear density distributions obtained from different parameter sets on the fusion mechanism, next the fusion and/or capture cross section for systems (a) ^{48}Ca + ^{248}Cm, (b) ^{26}Mg + ^{248}Cm, and (c) ^{58}Fe + ^{244}Pu is calculated within the ℓ-summed Wong model using nuclear potentials calculated by eight combinations of NN interaction and RMF density, namely NL1-NL1, NL1-NL3, NL1-TM1, NL1-DDME2, NL3-NL1, NL3-NL3, NL3-TM1, and NL3-DDME2, and plotted in Fig. 7 as functions of center-of-mass energy $E_{\text{c.m.}}$ (MeV). The available experimental data (black spheres) [69,70] are also given for

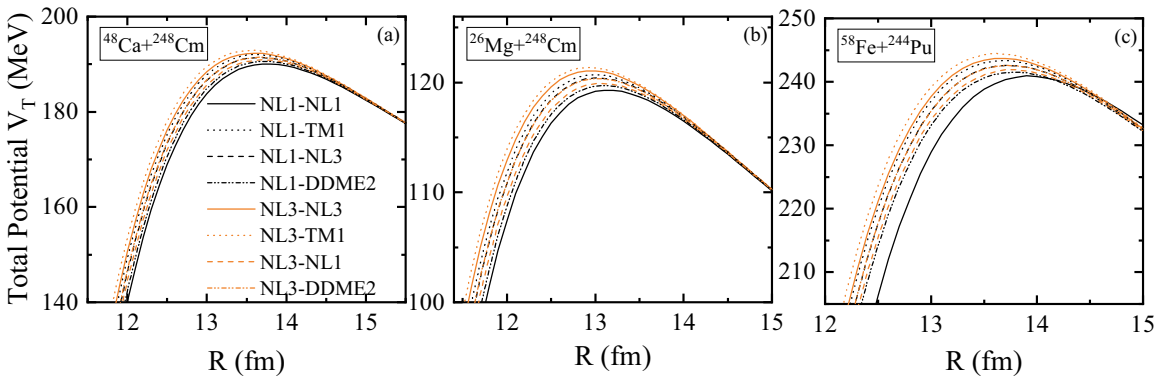

FIG. 6. The variation of total potential V_T (in MeV) as a function of radial distance R (in fm) for (a) ^{48}Ca + ^{248}Cm, (b) ^{26}Mg + ^{248}Cm, and (c) ^{58}Fe + ^{244}Pu calculated by fixing the NN potential for NL1 and NL3 parameter sets. NL3-TM1 signifies that the R3Y NN potential using the NL3 parameter set and density distributions using TM1 parameters within the folding procedures are used to obtain the nuclear potential. The same procedure is followed for other cases as labeled in the figure.

the comparison. Comparison of the cross sections calculated using different nuclear potentials shows that the TM1 density distributions decrease the cross section, whereas the NL1 densities increase the fusion and/or capture cross section. Also, the difference between the cross sections increases due to different nuclear potential at lower barrier energies. It becomes more prominent as we increase the mass number of the projectile nuclei. For the ^{26}Mg + ^{248}Cm [Fig. 7(b)] system, the plots of the cross section for different nuclear potentials almost overlap with each other, whereas a larger difference is observed for the ^{58}Fe + ^{244}Pu [Fig. 7(c)] system resulting in the formation of SHN $Z = 120$. This shows that the structure effects become more and more crucial as we move towards the heavier mass region of the periodic table. Comparison between the experimental and theoretical data shows that, for the ^{26}Mg + ^{248}Cm system, the NL1-NL1 combination is observed to be more suitable than the others. However, for the case of ^{48}Ca + ^{248}Cm, a nice fit is observed for NL3-TM1 with

TABLE I. The barrier position R_B (in fm) and barrier height V_B (in MeV) for all 24 considered reactions obtained by fixing one effective NN interaction and varying the nuclear density distributions. NL1-NL3 signifies that the R3Y NN potential obtained for the NL1 parameter set is folded with the RMF densities obtained for the NL3 parameter set.

	NL1-NL1		NL1-NL3		NL1-TM1		NL1-DDME2		NL3-NL3		NL3-NL1		NL3-TM1		NL3-DDME2	
System	R_B	V_B	R_B	V_B	R_B	V_B	R_B	V_B	R_B	V_B	R_B	V_B	R_B	V_B	R_B	V_B
^{31}Al + ^{197}Au	12.8	108.63	12.7	109.56	12.7	109.88	12.8	108.99	12.7	110.13	12.8	109.18	12.6	110.45	12.7	109.53
^{39}K + ^{181}Ta	12.8	147.56	12.7	148.67	12.8	148.94	12.7	147.99	12.6	149.44	12.7	148.31	12.6	149.90	12.7	148.72
^{46}K + ^{181}Ta	13.0	144.60	12.9	145.73	12.9	146.15	13.0	145.03	12.9	146.44	13.0	145.28	12.8	146.85	12.9	145.71
^{64}Ni + ^{238}U	13.9	253.12	13.8	254.91	13.7	255.69	13.8	253.80	13.7	255.98	13.8	254.14	13.7	256.76	13.8	254.82
^{48}Ca + ^{238}U	13.6	183.85	13.5	185.22	13.5	185.79	13.6	184.38	13.5	186.09	13.6	184.68	13.4	186.65	13.5	185.20
^{48}Ca + ^{154}Sm	12.7	133.44	12.5	134.64	12.5	135.15	12.6	133.90	12.5	135.34	12.6	134.11	12.4	135.85	12.5	134.56
^{48}Ca + ^{248}Cm	13.8	190.08	13.7	191.46	13.6	191.99	13.7	190.60	13.6	192.34	13.7	190.92	13.6	192.87	13.7	191.44
^{26}Mg + ^{248}Cm	13.1	119.30	13.0	120.42	13.0	120.71	13.1	119.73	13.1	120.96	13.1	119.93	12.9	121.37	13.0	120.35
^{40}Ca + ^{257}Fm	13.6	200.59	13.5	201.97	13.5	202.51	13.5	201.12	13.4	202.93	13.5	201.53	13.4	203.51	13.5	202.05
^{46}Ti + ^{248}Cf	13.5	216.61	13.5	218.21	13.4	218.87	13.5	217.23	13.4	219.25	13.5	217.62	13.4	219.90	13.5	218.21
^{46}Ti + ^{249}Cf	13.6	216.26	13.5	217.84	13.4	218.47	13.5	216.85	13.4	218.86	13.5	217.24	13.4	219.51	13.5	217.85
^{48}Ca + ^{254}Fm	13.8	197.58	13.7	199.01	13.7	199.55	13.8	198.10	13.6	199.90	13.7	198.43	13.6	200.48	13.7	199.00
^{50}Cr + ^{242}Cm	13.5	232.12	13.4	233.90	13.4	234.60	13.5	232.79	13.4	235.00	13.5	233.17	13.3	235.72	13.4	233.87
^{50}Ti +^{249} Cf	13.7	214.40	13.6	215.99	13.6	216.58	13.7	214.99	13.5	216.98	13.6	215.35	13.5	217.61	13.6	215.98
^{50}Ti + ^{252}Cf	13.8	213.32	13.7	214.88	13.6	215.46	13.7	213.91	13.6	215.88	13.7	214.28	13.6	216.46	13.7	214.88
^{54}Cr + ^{248}Cm	13.8	227.41	13.7	229.06	13.7	229.69	13.8	228.02	13.6	230.06	13.7	228.37	13.6	230.73	13.7	229.02
^{58}Fe + ^{244}Pu	13.8	240.88	13.7	242.62	13.7	243.34	13.8	241.53	13.7	243.69	13.8	241.89	13.6	244.43	13.7	242.57
^{64}Ni + ^{235}U	13.8	254.33	13.7	256.17	13.7	256.97	13.8	255.01	13.7	257.22	13.8	255.33	13.7	257.98	13.7	256.07
^{66}Ni + ^{236}U	13.9	252.59	13.8	254.33	13.8	255.06	13.9	253.23	13.7	255.30	13.8	253.52	13.7	256.08	13.8	254.21
^{50}Ti + ^{254}Cf	13.8	212.65	13.7	214.18	13.7	214.74	13.8	213.22	13.7	215.15	13.7	213.57	13.6	215.74	13.7	214.18
^{54}Cr + ^{250}Cm	13.8	226.68	13.7	228.25	13.7	228.89	13.8	227.26	13.7	229.28	13.8	227.61	13.6	229.90	13.7	228.22
^{60}Fe + ^{244}Pu	13.9	239.54	13.8	241.25	13.8	241.98	13.9	240.17	13.7	242.27	13.8	240.51	13.7	243.05	13.8	241.19
^{72}Zn + ^{232}Th	14.0	263.01	13.9	264.78	13.9	265.53	13.9	263.65	13.8	265.71	13.9	263.90	13.8	266.52	13.9	264.60
^{76}Ge + ^{228}Ra	14.0	274.19	13.9	276.06	13.9	276.89	14.0	274.87	13.9	277.05	13.9	275.12	13.8	277.93	13.9	275.87

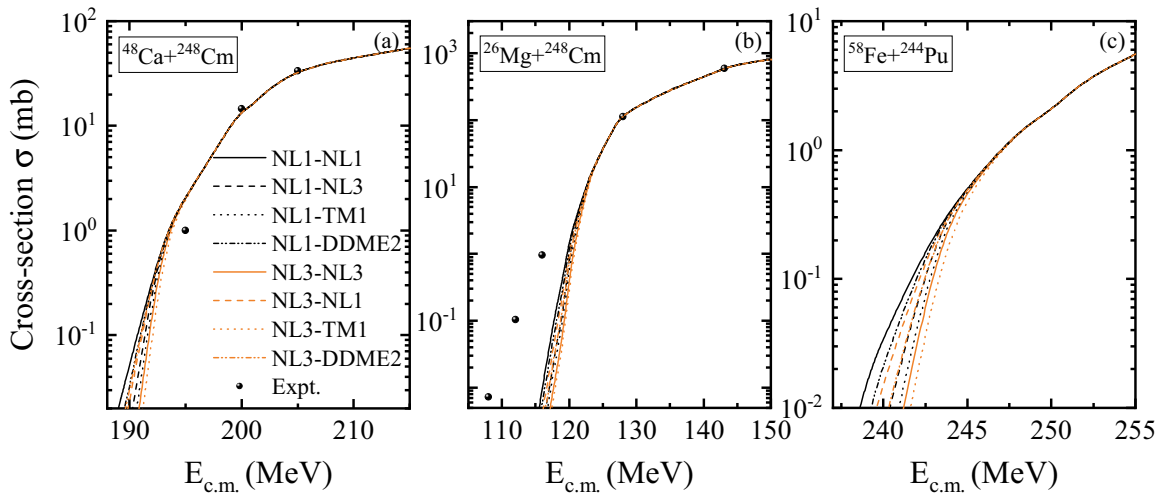

FIG. 7. The cross section σ (mb) calculated with the ℓ-summed Wong model using the R3Y NN potential for (a) ^{48}Ca + ^{248}Cm, (b) ^{26}Mg + ^{248}Cm, and (c) ^{58}Fe + ^{244}Pu. NL3-TM1 signifies that the R3Y NN potential using the NL3 parameter set and density distributions using the TM1 parameter set are used within the folding procedures to obtain the nuclear potential. The same procedure is followed for other cases as labeled in the figure.

the experimental cross section. All these observations indicate that even a small difference in the density distributions at the surface region significantly impacts the fusion and/or capture cross section. Also, this effect becomes more prominent as we move towards the superheavy region of the nuclear chart.

C. Fixing density and varying the R3Y NN potential

The double folding optical potential depends upon the nuclear density distributions and the effective nucleon-nucleon interaction. In the previous subsection, we investigated the effect of different nuclear density distributions on the optical nuclear potential and, consequently, on the fusion characteristics. To examine the effects of nucleon-nucleon (NN) interaction on the fusion barrier characteristics, we further fixed the nuclear densities and then changed the effective NN interaction in the double folding approach and studied the fusion characteristics. First, the R3Y NN interaction potential obtained for NL1, NL3, and TM1 parameter sets and the DDR3Y NN potential obtained for DDME2 parameter set are integrated over the nuclear densities obtained for the NL1 parameter set. Then the same procedure is repeated with densities obtained for the NL3 parameter set. Again we get eight nuclear potentials denoted as NL1-NL1, NL3-NL1, TM1-NL1, DDME2-NL1, NL1-NL3, NL3-NL3, TM1-NL3, and DDME2-NL3. All the notations have the same meanings as mentioned in the previous subsection. The calculations for the total interaction potential and the fusion and/or capture cross section are then carried out using these nuclear potentials.

1. Total interaction potential

Figure 8 displays the barrier region of the total interaction potential at $\ell = 0\hbar$ as a function of radial separation. As observed in the previous subsection, it is found here again that the NL1-NL1 combination gives the lowest value of the fusion barrier. The highest barrier is observed for the DDME2-NL3 combination, where the R3Y NN potential is density dependent. The inclusion of in-medium effects in microscopic the R3Y NN potential in terms of density-dependent nucleon-meson coupling parameters is observed to significantly raise the potential barrier. Also, the relativistic R3Y NN potential calculated with the TM1 parameter set, which accounts for the isoscalar vector ω meson's self-coupling, is observed to increase the potential barrier height compared to the NL3 and NL1 parameter sets. It is worth mentioning that the modification in the fusion barrier height caused by changing the effective NN interaction is comparatively more significant than the one observed by changing the density distributions. The values of barrier heights and positions for all 24 considered reactions systems are listed in Table II. On replacing the R3Y NN potential obtained for NL1 with that obtained for TM1 for a fixed density distribution, the barrier height increases by ≈1.5 MeV. The barrier height further increases by up to 5 MeV on replacing the R3Y NN potential obtained for the TM1 parameter set with the DDR3Y NN potential obtained for the DDME2 parameter set using the relaxed density approximation. This difference in the barrier heights given by R3Y and DDR3Y NN potentials is slightly more when folded with the NL3 density as compared with the NL1 density. Also the changes in the barrier characteristics w.r.t. the RMF parameter sets become more significant as the mass of the compound nucleus increases. For further exploration of the consequences of different relativistic force parameter sets in terms of NN potential, the fusion and/or capture cross section for all eight combinations of nuclear potential given in Fig. 8 are investigated.

2. Fusion and/or capture cross section

The fusion and/or capture cross section for the systems (a) ^{48}Ca + ^{248}Cm, (b) ^{26}Mg + ^{248}Cm, and (c) ^{58}Fe + ^{244}Pu is obtained as a function of center-of-mass energy and is represented in Fig. 9. The effect of the interaction potential

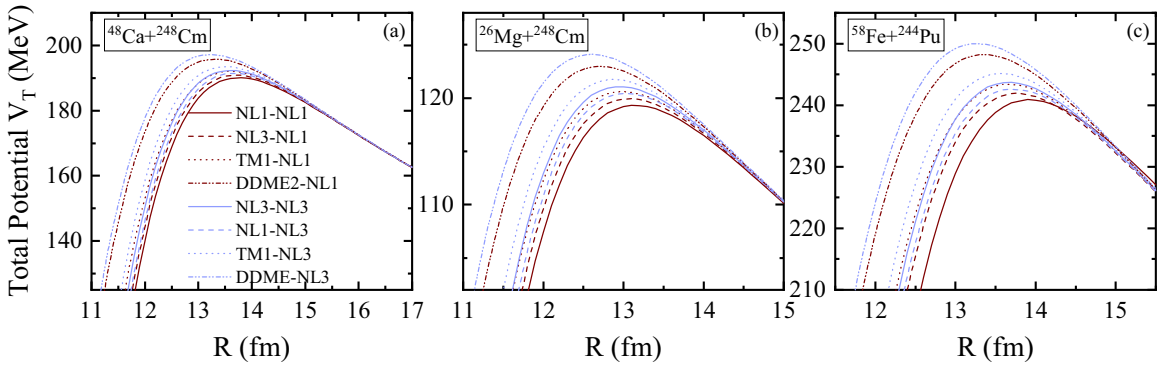

FIG. 8. The variation of total potential V_T (in MeV) as a function of radial distance R (in fm) for (a) ^{48}Ca + ^{248}Cm, (b) ^{26}Mg + ^{248}Cm, and (c) ^{58}Fe + ^{244}Pu calculated by fixing the density for NL1 and NL3 parameter sets. The notation NL3-NL1 signifies that the R3Y NN potential from the NL3 parameter set and density distributions from the NL1 parameters are used in the folding procedure to obtain the nuclear potential. The same procedure is followed for other cases as labeled in the figure.

characteristics are observed directly in the fusion and/or capture cross section. We obtained the highest cross section for the combination NL1-NL1, whereas the lowest cross section was observed for the DDME2-NL3 parameter set. Also, the DDR3Y NN potential obtained for the DDME2 parameter set gives a lower cross section compared to the medium-independent R3Y NN potential obtained for nonlinear NL1, NL3, and TM1 parameter sets. This indicates that the inclusion of in-medium effects in the microscopic NN potential decreases the cross section. The structure effects of the interaction potential are observed to be diminished at energies greater than the fusion barrier. For system ^{48}Ca + ^{248}Cm [Fig. 9(a)], the DDR3Y NN potential obtained for the DDME2 parameter set folded with the NL1 density give a better fit to the experimental data. However for a system with a lighter projectile, i.e., ^{26}Mg + ^{248}Cm [Fig. 9(b)], the parameter set NL1 gives better results. The effects of varying the effective

TABLE II. The barrier position R_B (in fm) and barrier height V_B (in MeV) for all 24 considered reactions obtained by fixing the nuclear density distributions and varying the NN interaction. TM1-NL1 signifies that the R3Y NN potentials obtained for the TM1 parameter set are folded with RMF densities obtained for the NL1 parameter set.

	TM1-NL1		DDME2-NL1		TM1-NL3		DDME2-NL3	
System	R_B	V_B	R_B	V_B	R_B	V_B	R_B	V_B
^{31}Al + ^{197}Au	12.7	109.85	12.4	112.07	12.6	110.79	12.3	113.00
^{39}K + ^{181}Ta	12.6	149.24	12.3	152.39	12.5	150.37	12.2	153.54
^{46}K + ^{181}Ta	12.9	146.19	12.6	149.21	12.8	147.34	12.5	150.36
^{64}Ni + ^{238}U	13.7	255.73	13.4	260.91	13.6	257.55	13.3	262.76
^{48}Ca + ^{238}U	13.5	185.78	13.2	189.40	13.4	187.18	13.1	190.84
^{48}Ca + ^{154}Sm	12.5	134.92	12.2	137.55	12.4	136.13	12.1	138.77
^{48}Ca + ^{248}Cm	13.6	192.07	13.3	195.78	13.5	193.47	13.2	197.20
^{26}Mg + ^{248}Cm	13.0	120.62	12.7	122.97	12.9	121.75	12.6	124.10
^{40}Ca + ^{257}Fm	13.4	202.77	13.1	206.64	13.3	204.15	13.0	208.04
^{46}Ti + ^{248}Cf	13.4	218.93	13.1	223.15	13.3	220.54	13.0	224.78
^{46}Ti + ^{249}Cf	13.4	218.55	13.1	222.77	13.3	220.15	13.0	224.38
^{48}Ca + ^{254}Fm	13.6	199.62	13.3	203.42	13.5	201.07	13.3	204.89
^{50}Cr + ^{242}Cm	13.4	234.56	13.1	239.13	13.3	236.37	13.0	240.96
^{50}Ti + ^{249}Cf	13.5	216.62	13.3	220.79	13.5	218.24	13.2	222.43
^{50}Ti + ^{252}Cf	13.6	215.56	13.3	219.71	13.5	217.15	13.2	221.31
^{54}Cr + ^{248}Cm	13.6	229.76	13.3	234.28	13.5	231.43	13.3	235.95
^{58}Fe + ^{244}Pu	13.7	243.37	13.4	248.19	13.6	245.15	13.3	249.99
^{64}Ni + ^{235}U	13.6	256.91	13.3	262.12	13.6	258.79	13.2	264.01
^{66}Ni + ^{236}U	13.7	255.14	13.4	260.41	13.6	256.90	13.3	262.22
^{50}Ti + ^{254}Cf	13.7	214.85	13.4	218.99	13.6	216.47	13.3	220.57
^{54}Cr + ^{250}Cm	13.7	229.01	13.4	233.51	13.6	230.66	13.3	235.17
^{60}Fe + ^{244}Pu	13.7	241.98	13.4	246.81	13.7	243.72	13.3	248.55
^{72}Zn + ^{232}Th	13.8	265.64	13.5	271.33	13.7	267.42	13.4	273.14
^{76}Ge + ^{228}Ra	13.8	276.92	13.5	282.85	13.7	278.81	13.4	284.75

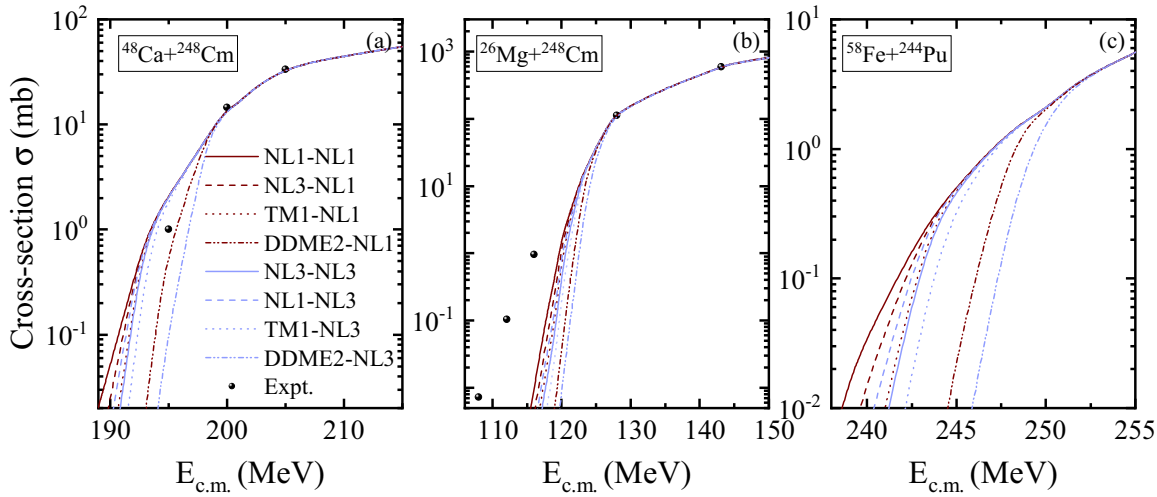

FIG. 9. The cross section σ (mb) calculated with the ℓ-summed Wong model using the R3Y NN potential for (a) ^{48}Ca + ^{248}Cm, (b) ^{26}Mg + ^{248}Cm, and (c) ^{58}Fe + ^{244}Pu. First, the NL1 density is folded with all four parameter sets (NL1, NL3, TM1, and DDME2), and then the procedure is repeated for the NL3 density. NL3-NL1 signifies that the R3Y NN potential from the NL3 parameter set and density distributions from the NL1 parameters within the folding procedure are used to obtain the nuclear potential. The same procedure is followed for other cases as labeled in the figure.

NN interaction are observed to be more prominent than those of the nuclear density distributions.

Comparing the barrier characteristics and the fusion and/or capture cross sections obtained for M3Y and R3Y NN potentials folded with nuclear density distributions for four different parameters sets, it is concluded that relativistic R3Y NN potentials give a better prediction to the experimental data. Also, as compared to the TM1 and DDME2 parameter sets, which were introduced to include the self-coupling of the vector ω mesons and density dependence of nucleon-meson couplings, respectively [44,61], the NL1 and NL3 parameter sets give better overlap with the experimental data for the fusion and/or capture cross section. Moreover, NL1 is superior to NL3 in addressing the experimental cross sections. However, in the case of nuclear matter properties, the NL1 parameter set produces a large value of the asymmetry parameter [42,43]. Moreover the NL1 parameter set also fails to fit the neutron skin thickness of the nuclei away from the β-stability line [58,59]. On the other hand, the parameter set NL3 improves the value of the asymmetry parameter without increasing the number of phenomenological parameters. In the present study, the NL3 parameter set gives a better fit to the fusion and/or capture cross section as compared to the TM1 parameter set, which includes the self-coupling terms of the vector meson in the RMF Lagrangian [44]. Taking all these facts into account, it can be concluded that the parameter set NL3 is suitable for describing the bulk and fusion characteristics of finite nuclei (including heavy and superheavy nuclei with higher N/Z ratio) and properties of infinite nuclear matter. The TM1 parameter set, which was introduced to incorporate the vector self-coupling to soften the equation of state of nuclear matter [44], gives a comparatively repulsive nuclear potential in terms of nuclear density distributions and the effective NN interaction potential, which consequently underestimates the fusion and/or capture cross section. The inclusion of density dependence in the R3Y NN potential within the relativistic Hartree-Bogoliubov approach for the DDME2 parameter set is observed to decrease the cross section w.r.t. the density-independent R3Y NN potentials obtained for NL1, NL3, and TM1 parameter sets. In the present analysis, we have considered only the isospin asymmetric reaction systems, i.e., target-projectile combinations forming a neutron-rich compound nucleus. A systematic study with isospin symmetric ($N = Z$) reaction systems will be carried out in the near future.

IV. SUMMARY AND CONCLUSIONS

A systematic study is carried out in order to study the effect of nuclear density distributions and the effective NN interaction on the fusion barrier characteristics. The fusion barrier properties and cross section of 24 different target-projectile combinations containing the even-even ^{48}Ca + ^{154}Sm, ^{48}Ca + ^{238}U, ^{48}Ca + ^{248}Cm, ^{26}Mg + ^{248}Cm; even-odd ^{46}K + ^{181}Ta; and odd-odd ^{31}Al + ^{197}Au and ^{39}K + ^{181}Ta systems as well as systems leading to the synthesis of superheavy isotopes of $Z = 120$, ^{40}Ca + ^{257}Fm, ^{48}Ca + ^{254}Fm, ^{46}Ti + ^{248}Cf, ^{46}Ti + ^{249}Cf, ^{50}Ti + ^{249}Cf, ^{50}Ti + ^{252}Cf, ^{50}Cr + ^{242}Cm, ^{54}Cr + ^{248}Cm, ^{58}Fe + ^{244}Pu, ^{64}Ni + ^{238}U, ^{64}Ni + ^{235}U, ^{66}Ni + ^{236}U, ^{50}Ti + ^{254}Cf, ^{54}Cr + ^{250}Cm, ^{60}Fe + ^{244}Pu, ^{72}Zn + ^{232}Th, and ^{76}Ge + ^{228}Ra, are investigated within the relativistic mean field formalism. The nuclear density distributions for all the interacting nuclei are obtained by employing the RMF formalism for NL1, NL3, TM1 parameter sets and the RHB approach for the DDME2 parameter set. The effective NN interactions are obtained using the well-known M3Y potential and the relativistic R3Y and DDR3Y potentials. The R3Y NN potential is obtained for the three considered relativistic mean-field parameter sets (NL1, NL3, and TM1) and the DDR3Y NN potential is obtained within the RHB approach for the DDME2 parameter set.

In the first step, the comparison of M3Y, R3Y, and DDR3Y NN potentials is carried out by calculating the fusion barrier characteristics using the nuclear potential within the double folding approach. It is concluded that the relativistic R3Y and DDR3Y NN interaction potentials give a relatively better fit to the experimental data than the M3Y potential. It is also observed that the NL1 and NL3 parameter sets give a better fit to the experimental data than the TM1 and DDME2 parameter sets. However for systems $^{46}K + ^{181}Ta$, $^{48}Ca + ^{248}Cm$, and $^{64}Ni + ^{238}U$, the TM1 parameter set works better. Second, the effective NN interaction is fixed, and then the nuclear density distributions are changed in the folding procedure to study their effect on the fusion characteristics. It is noticed that the nuclear densities obtained for parameter sets NL3, TM1, and DDME2 give comparatively repulsive nuclear potentials and consequently decrease the fusion and/or capture cross section. In the last step, we studied the effects of the effective NN interaction on the fusion characteristics by fixing the nuclear densities. We find that the TM1 parameter set gives a repulsive R3Y NN interaction potential and thus decreases the fusion probability. All these observations lead to the conclusion that the inclusion of the vector self-coupling term ($\propto \omega^4$) in the RMF Lagrangian increases the magnitude of the repulsive core of the NN interaction, which consequently underestimates the cross section. Moreover, the DDR3Y NN potential calculated in terms of density-dependent nucleon-meson couplings within the relativistic Hartree-Bogoliubov (RHB) approach for the DDME2 parameter set is observed to give a higher barrier height and lower fusion cross section as compared to the medium-independent R3Y NN potential obtained within the RMF formalism for NL1, NL3 and TM1 parameter sets. From the comparison of the theoretical cross section with the available experimental data, it is concluded that both the densities and R3Y NN potential obtained for NL1 and NL3 parameters give comparatively better overlap than the TM1 and DDME2 parameter sets. However, if we consider the overall description of bulk properties and fusion characteristics of finite nuclei and the properties of infinite nuclear matter, the NL3 becomes the favorable choice. It is worth mentioning that the shape degrees of freedom, i.e., the nuclear deformations for the interacting nuclei, are not considered in the present analysis. Hence, the results may change slightly without affecting the predictions by including nuclear shape degrees of freedom within the relativistic mean-field formalism, which will be carried out shortly.

ACKNOWLEDGMENTS

This work was supported by the Board of Research in Nuclear Sciences (BRNS), Sanction No. 58/14/12/2019-BRNS, Science Engineering Research Board (SERB), File No. CRG/2021/001229, FOSTECT Project Code FOSTECT.2019B.04, and FAPESP Project No. 2017/05660-0.

[1] G. Montagnoli and A. M. Stefanini, Eur. Phys. J. A **53**, 169 (2017).
[2] K. Cheng and C. Xu, Nucl. Phys. A **992**, 121642 (2019).
[3] L. F. Canto, V. Guimaraes, J. Lubian, and M. S. Hussein, Eur. Phys. J. A **56**, 281 (2020).
[4] A. J. Toubiana, L. F. Canto, and M. S. Hussein, Braz. J. Phys. **47**, 321 (2017).
[5] A. Wakhle, K. Hammerton, Z. Kohley, D. J. Morrissey, K. Stiefel, J. Yurkon, J. Walshe, K. J. Cook, M. Dasgupta, D. J. Hinde, D. J. Jeung, E. Prasad, D. C. Rafferty, C. Simenel, E. C. Simpson, K. Vo-Phuoc, J. King, W. Loveland, and R. Yanez, Phys. Rev. C **97**, 021602(R) (2018).
[6] M. Dasgupta, D. J. Hinde, N. Rowley, and A. M. Stefanini, Annu. Rev. Nucl. Part. Sci. **48**, 401 (1998).
[7] V. L. Litnevsky, F. A. Ivanyuk, G. I. Kosenko, and S. Chiba, Phys. Rev. C **101**, 064616 (2020).
[8] F. Ghorbani, S. A. Alavi, V. Dehghani, A. Soylu, and F. Koyuncu, Phys. Rev. C **102**, 014610 (2020).
[9] E. M. Kozulin, G. N. Knyazheva, K. V. Novikov, I. M. Itkis, M. G. Itkis, S. N. Dmitriev, Y. T. Oganessian, A. A. Bogachev, N. I. Kozulina, I. Harca, W. H. Trzaska, and T. K. Ghosh, Phys. Rev. C **94**, 054613 (2016).
[10] R. N. Sahoo, M. Kaushik, A. Sood, A. Sharma, S. Thakur, P. Kumar, M. M. Shaikh, R. Biswas, A. Yadav, M. K. Sharma, J. Gehlot, S. Nath, N. Madhavan, R. G. Pillay, E. M. Kozulin, G. N. Knyazheva, K. V. Novikov, and P. P. Singh, Phys. Rev. C **102**, 024615 (2020).
[11] I. Dutt and R. K. Puri, Phys. Rev. C **81**, 064608 (2010).
[12] O. N. Ghodsi and F. Lari, Mod. Phys. Lett. A **28**, 1350116 (2013).
[13] H. C. Manjunatha and K. N. Sridhar, Nucl. Phys. A **971**, 83 (2018).
[14] L. F. Canto, P. R. S. Gomes, R. Donangelo, and M. S. Hussein, Phys. Rep. **424**, 1 (2006).
[15] B. B. Back, H. Esbensen, C. L. Jiang, and K. E. Rehm, Rev. Mod. Phys. **86**, 317 (2014).
[16] J. Błocki, J. Randrup, W. J. Swiatecki, and C. F. Tsang, Ann. Phys. (NY) **105**, 427 (1977).
[17] J. Blocki and W. J. Swiatecki, Ann. Phys. (NY) **132**, 53 (1981).
[18] R. Kumar, Phys. Rev. C **84**, 044613 (2011).
[19] D. Jain, R. Kumar, and M. K. Sharma, Nucl. Phys. A **915**, 106 (2013).
[20] R. Bass, Phys. Lett. B **47**, 139 (1973).
[21] R. Bass, Nucl. Phys. A **231**, 45 (1974).
[22] R. Bass, Phys. Rev. Lett. **39**, 265 (1977).
[23] D. Vautherin and D. M. Brink, Phys. Rev. C **5**, 626 (1972).
[24] R. Kumar, M. K. Sharma, and R. K. Gupta, Nucl. Phys. A **870–871**, 42 (2011).
[25] D. Jain, M. K. Sharma, Rajni, R. Kumar, and R. K. Gupta, Eur. Phys. J. A **50**, 155 (2014).
[26] *Nuclear Structure Physics*, edited by A. Shukla and S. K. Patra (CRC, Boca Raton, FL, 2020), Chap. 5.
[27] J. Maruhn and W. Greiner, Z. Phys. **251**, 431 (1972).
[28] B. Grammaticos and A. Voros, Ann. Phys. (NY) **123**, 359 (1979).
[29] B. Grammaticos and A. Voros, Ann. Phys. (NY) **129**, 153 (1980).
[30] M. Brack, C. Guet and H.-B. Hakansson, Phys. Rep. **123**, 275 (1985).

[31] M. Dutra, O. Lourenço, J. S. Sá Martins, A. Delfino, J. R. Stone, and P. D. Stevenson, Phys. Rev. C **85**, 035201 (2012).
[32] G. R. Satchler and W. G. Love, Phys. Rep. **55**, 183 (1979).
[33] G. Bertsch, J. Borysowicz, H. McManus, and W. G. Love, Nucl. Phys. A **284**, 399 (1977).
[34] D. T. Khoa, N. H. Phuc, D. T. Loan, and B. M. Loc, Phys. Rev. C **94**, 034612 (2016).
[35] Z. Gao-Long and L. Xiao-Yun, Chin. Phys. C **32**, 812 (2008).
[36] M. Bhuyan and R. Kumar, Phys. Rev. C **98**, 054610 (2018).
[37] M. Bhuyan, R. Kumar, S. Rana, D. Jain, S. K. Patra, and B. V. Carlson, Phys. Rev. C **101**, 044603 (2020).
[38] B. B. Singh, M. Bhuyan, S. K. Patra, and R. K. Gupta, J. Phys. G: Nucl. Part. Phys. **39**, 025101 (2012).
[39] B. B. Sahu, S. K. Singh, M. Bhuyan, S. K. Biswal, and S. K. Patra, Phys. Rev. C **89**, 034614 (2014).
[40] C. Lahiri, S. K. Biswal, and S. K. Patra, Int. J. Mod. Phys. E **25**, 1650015 (2016).
[41] M. Bhuyan and S. K. Patra, Mod. Phys. Lett. A **27**, 1250173 (2012).
[42] P.-G. Reinhard, M. Rufa, J. Maruhn, W. Greiner, and J. Friedrich, Z. Physik A - Atom. Nuclei **323**, 13 (1986).
[43] G. A. Lalazissis, J. Konig, and P. Ring, Phys. Rev. C **55**, 540 (1997).
[44] A. R. Bodmer, Nucl. Phys. A **526**, 703 (1991).
[45] D. Vretenar, A. V. Afanasjev, G. A. Lalazissis, and P. Ring, Phys. Rep. **409**, 101 (2005).
[46] *Relativistic Density Functional for Nuclear Structure*, edited by J. Meng, International Review of Nuclear Physics, Vol. 10 (World Scientific, Singapore, 2016).
[47] P. Ring, Prog. Part. Nucl. Phys. **37**, 193 (1996).
[48] A. Taninah, S. E. Agbemava, and A. V. Afanasjev, Phys. Rev. C **102**, 054330 (2020).
[49] R. K. Gupta, S. K. Patra, and W. Greiner, Mod. Phys. Lett. A **12**, 23 (1997).
[50] R. J. Furnstahl, B. D. Serot, and H. Tang, Nucl. Phys. A **615**, 441 (1997).
[51] B. Kumar, S. K. Singh, B. K. Agrawal, and S. K. Patra, Nucl. Phys. A **966**, 197 (2017).
[52] B. Kumar, S. K. Patra, and B. K. Agrawal, Phys. Rev. C **97**, 045806 (2018).
[53] S. Typel and H. H. Wolter, Nucl. Phys. A **656**, 331 (1999).
[54] C. Fuchs, H. Lenske, and H. H. Wolter, Phys. Rev. C **52**, 3043 (1995).
[55] T. Nikšić, D. Vretenar, P. Finelli, and P. Ring, Phys. Rev. C **66**, 024306 (2002).
[56] J. Meng, H. Toki, S. G. Zhou, S. Q. Zhang, W. H. Long, and L. S. Geng, Prog. Part. Nucl. Phys. **57**, 470 (2006).
[57] W. Zhang, J. Meng, S. Q. Zhang, L. S. Geng, and H. Toki, Nucl. Phys. A **753**, 106 (2005).
[58] A. V. Afanasjev, J. König, and P. Ring, Nucl. Phys. A **608**, 107 (1996).
[59] A. V. Afanasjev, J. König, and P. Ring, Phys. Lett. B **367**, 11 (1996).
[60] F. Hofmann, C. M. Keil, and H. Lenske, Phys. Rev. C **64**, 034314 (2001).
[61] G. A. Lalazissis, T. Niksic, D. Vretenar, and P. Ring, Phys. Rev. C **71**, 024312 (2005).
[62] M. Bhuyan, Phys. Rev. C **92**, 034323 (2015).
[63] M. Bhuyan, B. V. Carlson, S. K. Patra, and S.-G. Zhou, Phys. Rev. C **97**, 024322 (2018).
[64] B. Kumar and P. Landry, Phys. Rev. D **99**, 123026 (2019).
[65] M. Dutra, O. Lourenço, S. S. Avancini, B. V. Carlson, A. Delfino, D. P. Menezes, C. Providência, S. Typel, and J. R. Stone, Phys. Rev. C **90**, 055203 (2014).
[66] M. Bhuyan, S. Rana, R. Kumar, and S. K. Patra, arXiv:2204.05993.
[67] Y. X. Watanabe *et al.*, Eur. Phys. J. A **10**, 373 (2001).
[68] G. N. Knyazheva, E. M. Kozulin, R. N. Sagaidak, A. Y. Chizhov, M. G. Itkis, N. A. Kondratiev, V. M. Voskressensky, A. M. Stefanini, B. R. Behera, L. Corradi, E. Fioretto, A. Gadea, A. Latina, S. Szilner, M. Trotta, S. Beghini, G. Montagnoli, F. Scarlassara, F. Haas, N. Rowley, P. R. S. Gomes, and A. Szantode Toledo, Phys. Rev. C **75**, 064602 (2007).
[69] M. G. Itkis *et al.*, Nucl. Phys. A **734**, 136 (2004).
[70] E. V. Prokhorova *et al.*, in *Proceedings of the International Symposium on Exotic Nuclei (EXON2004), Peterhof, Russian Federation, July 52, 2004*, edited by Y. E. Penionzhkevich and E. A. Cherepanov (World Scientific, Singapore, 2005), p. 325.
[71] E. M. Kozulin *et al.*, Phys. Lett. B **686**, 227 (2010).
[72] G. G. Adamian, N. V. Antonenko, and V. V. Sargsyan, Phys. Rev. C **79**, 054608 (2009).
[73] S. Hofmann *et al.*, Nucl. Phys. A **734**, 93 (2004).
[74] A. Sobiczewski, F. A. Gareev, and B. N. Kalinkin, Phys. Lett. **22**, 500 (1966).
[75] S. G. Nilsson, C. F. Tsang, A. Sobiczewski, Z. Szymanski, S. Wycech, C. Gustafson, I. N. Lamm, P. Moller, and B. Nilsson, Nucl. Phys. A **131**, 1 (1969).
[76] G. A. Lalazissis, M. M. Sharma, P. Ring, and Y. K. Gambhir, Nucl. Phys. A **608**, 202 (1996).
[77] K. Rutz, M. Bender, T. Burvenich, T. Schilling, P.-G. Reinhard, J. A. Maruhn, and W. Greiner, Phys. Rev. C **56**, 238 (1997).
[78] S. E. Agbemava, A. V. Afanasjev, T. Nakatsukasa, and P. Ring, Phys. Rev. C **92**, 054310 (2015).
[79] R. Kumar, M. Bansal, S. K. Arun, and R. K. Gupta, Phys. Rev. C **80**, 034618 (2009).
[80] V. Yu. Denisov, Phys. Rev. C **88**, 044608 (2013).
[81] V. Yu. Denisov, Phys. Rev. C **91**, 024603 (2015).
[82] A. M. Kobos, B. A. Brown, P. E. Hodgson, G. R. Sstchler, and A. Budzsnowski, Nucl. Phys. A **384**, 65 (1982).
[83] D. T. Khoa, W. von Oertzen, and H. G. Bohlen, Phys. Rev. C **49**, 1652 (1994).
[84] J. Y. Zeng and T. S. Cheng, Nucl. Phys. A **405**, 1 (1983).
[85] H. Molique and J. Dudek, Phys. Rev. C **56**, 1795 (1997).
[86] J. Dobaczewski, H. Flocard, and J. Treiner, Nucl. Phys. A **422**, 103 (1984).
[87] D. G. Madland and J. R. Nix, Nucl. Phys. A **476**, 1 (1988).
[88] C. Y. Wong, Phys. Rev. Lett. **31**, 766 (1973).
[89] D. L. Hill and J. A. Wheeler, Phys. Rev. **89**, 1102 (1953).
[90] P.-G. Reinhard, M. Bender, and J. A. Maruhn, Comments Mod. Phys. **2**, A177 (2002).
[91] A. V. Afanasjev and S. Frauendorf, Phys. Rev. C **71**, 024308 (2005).
[92] Y. Chu, Z. Ren, Z. Wang, and T. Dong, Phys. Rev. C **82**, 024320 (2010).
[93] R. K. Gupta, D. Singh, and W. Greiner, Phys. Rev. C **75**, 024603 (2007).
[94] S. Rana, R. Kumar, and M. Bhuyan, Phys. Rev. C **104**, 024619 (2021).
[95] M. Beckerman, J. Ball, H. Enge, M. Salomaa, A. Sperduto, S. Gazes, A. DiRienzo, and J. D. Molitoris, Phys. Rev. C **23**, 1581 (1981).